ICT Project No 871813
MUNDFAB
Modeling Unconventional Nanoscaled
Device FABrication

D3.6 Final version of KMC process models calibrated with experiments

Public version

S. Mundinar (Fraunhofer), C. Rossi (Fraunhofer), P. Pichler (Fraunhofer), A. Johnsson (Fraunhofer), D. Raciti (CNR), G. Calogero (CNR), D. Ricciarelli (CNR), I. Deretzis (CNR), G. Fisicaro (CNR), A. La Magna (CNR), B. Martínez I Diaz (CEA), L. Treps (CEA), J. Li (CEA), B. Sklénard (CEA)

August 22, 2023

Quality management

This deliverable was reviewed by:

Paweł MICHAŁOWSKI (Ł-IMiF)

Richard DAUBRIAC (CNRS)

Contents

Abbreviations

4PP	4-Point Probe measurements
CI-NEB	Climbing Image Nudged Elastic Band method
CVD	Chemical Vapor Deposition
DCS	Dichlorosilane
DFT	Density Functional Theory
FS	Final State
IS	Initial State
KMC	Kinetic Monte Carlo
KMCsL	super-Lattice Kinetic Monte Carlo
LA	Laser Annealing
LKMC	Lattice Kinetic Monte Carlo
MC	Monte Carlo
PVD	Physical Vapor Deposition
RPA	Random Phase Approximation
SE	Spectroscopic Ellipsometry
SIMS	Secondary Ion Mass Spectrometry
TS	Transition State
XRD	X-Ray Diffraction Analysis
XRR	X-Ray Reflectometry

Abstract

In this deliverable, the final versions of kinetic Monte Carlo (KMC) process models for the simulation of epitaxial growth and post-epitaxy annealing are presented. Epitaxial growth simulations are calibrated based on experimental data obtained from literature and within the MUNDFAB project, as well as *ab initio* simulations for specific precursors. Presented here, are such simulations for H coverage and Si(001) surface reactions with SiH_4 and HCl. Corresponding to the two strategies adopted in the MUNDFAB project, epitaxial growth is treated in parallel using the lattice KMC models implemented in the commercial Sentaurus TCAD software and the open-source software package `MulSKIPS`. The calibration within Sentaurus TCAD focuses on specific precursors that are crucial for the epitaxy of *in-situ* doped SiGe layers. Within `MulSKIPS`, the reactions for similar precursors are calibrated, but including gas-phase reactions of the precursors using the Cantera software package. Finally, post-epitaxy annealing is discussed again within Sentaurus TCAD.

1. Introduction

Work Package 3 (WP3) is dedicated to investigating epitaxial growth by chemical vapor deposition, as well as *in situ* doping, and post-epitaxy annealing. Epitaxial growth by chemical vapor deposition is a widely used method during manufacturing nanoelectronic devices, like e.g., FinFETs and FDSOI devices including two of the test applications from WP6. The goal of this deliverable D3.6 is to demonstrate the final theoretical models obtained within the MUNDFAB project that are used to simulate growth rates, mole fractions, and doping concentrations. This includes *ab initio* simulations for the adsorption of different precursors, as well as Lattice Kinetic Monte Carlo (LKMC) simulations for the epitaxial growth. In addition, simulations for the post-epitaxy laser annealing are presented.

The remainder of this deliverable is structured as follows: In Section 2 *ab initio* simulations are carried out for the Si(001) surface reactions with hydrogen, silane and for HCl. These will act as a guide for the calibration of LKMC models for epitaxial growth. In Section 2.3 the final models for epitaxial growth within Synopsys Sentaurus TCAD are demonstrated and in Section 4 the final models for the epitaxial growth using `MulSKIPS` are shown. Finally, in Section 5 a model for post-epitaxial annealing is discussed and results are shown.

2. *Ab initio* simulations of surface reactions on Si(001)

2.1 Si(001) H coverage

In deliverable D3.4 we presented a thermodynamic model to study the H coverage of a Si(001). Some preliminary results were shown using PBE+D3, and HSE06 exchange correlation functional. Here we report new results including a configurational entropy. We also employ the more advanced Random Phase Approximation (RPA) calculation (i.e., from the adiabatic connection fluctuation dissipation theorem) to compute the correlation energy E_c. The total ground state energy is obtained by summing this correlation energy to the Hartree-Fock energy E_x: $E_{tot} = E_c + E_x$.

We considered (4×2) Si(001) slabs with various H coverages from θ=0 ML to θ=2 ML. For each coverage, ground state energy calculations were performed at the PBE+D3, HSE06 or RPA level, while phonon calculations were done at the PBE+D3 level only to evaluate the vibrational entropy contribution.

For a system with microstates i the configurational entropy is given by:

$$S_{conf}(T) = -k_B \sum_i P_i(T) \ln P_i(T)$$

where:

$$P_i(T) = \frac{1}{Z_i} \exp(-\beta E_i)$$

with Z_i the partition function, $\beta = (k_B T)^{-1}$ and E_i the energy of state i. A direct evaluation of the configurational entropy is usually computationally not tractable. Here we drastically simplified the problem by considering the 13 different configurations corresponding to H adsorption on a single Si–Si dimer (computed at the PBE+D3 level), assuming that neighboring dimers will have a negligible influence. Then we computed the configuration entropy for each

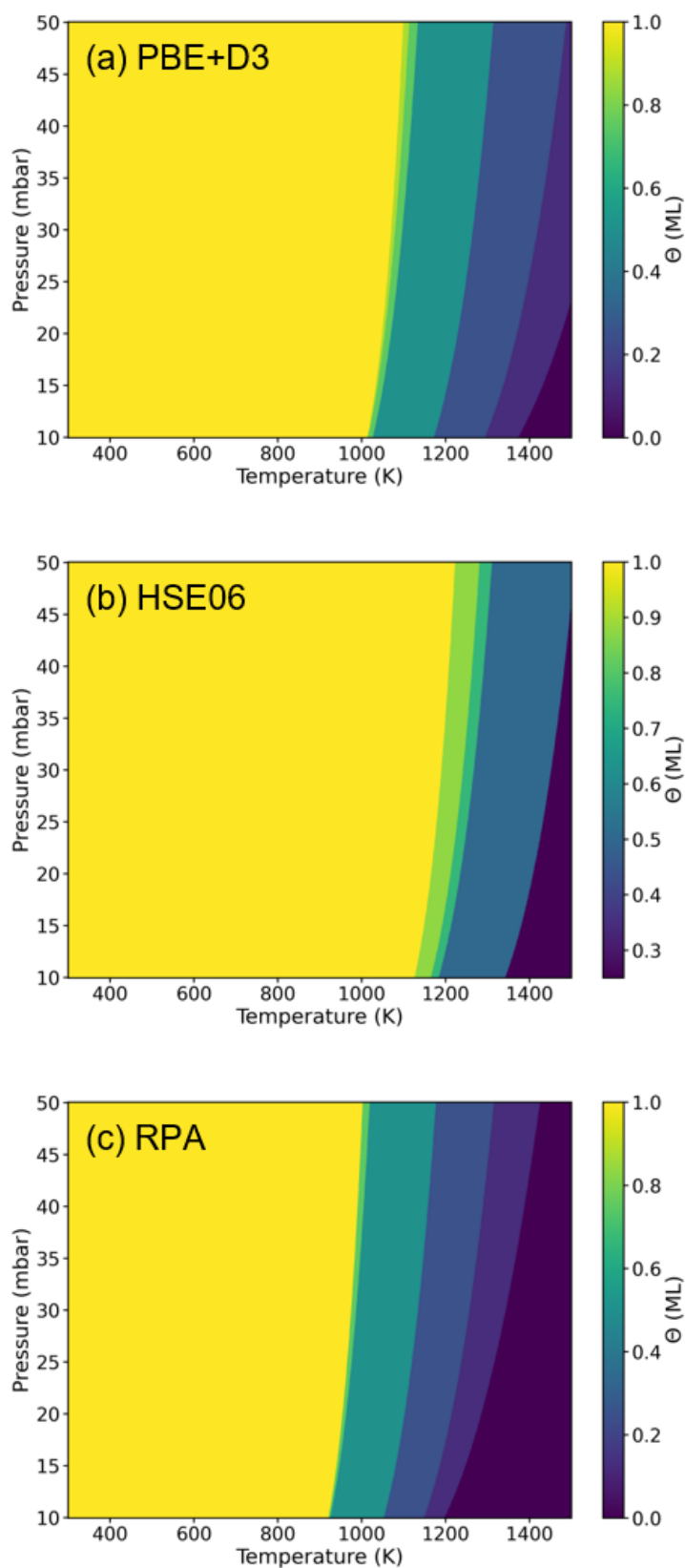coverage. We expect that the computed configurational entropy is more accurate than in Ref. [1].

Figure 1: Most stable H coverage as a function of temperature and pressure computed at (a) PBE+D3 (b) HSE06 and (c) RPA level.

The temperature and pressure dependent most stable H coverage is obtained from the minimum of the free energy differences (see deliverable D3.4). The results for each method are summarized in Figure 1. For all methods, the θ=1 ML (θ=0 ML) is predicted to be the most stable at low (high) temperatures, in good agreement with experimental observations. The transition temperature between these two coverages varies depending on the calculation method but RPA should be considered as the reference. Intermediate coverages are stable due to the configurational entropy (which is maximum for θ=0.5 ML). For the considered pressure and temperature ranges, θ>1 ML H coverages were not found to be thermodynamically stable as it involves breaking a Si–Si dimer.

2.2 Adsorption of Silane

As discussed in the previous section, H coverage may vary on a Si(001) surface, depending on the epitaxy process conditions (temperature and H_2 partial pressure). This may have a strong impact on the growth kinetics of the different precursors. In particular, for process conditions corresponding to a low temperature epitaxy, Si–Si dimers at the surface are fully passivated by H (i.e., $\Theta \sim$ 1ML) which limits the adsorption of precursors.

We studied the impact of H coverage on the adsorption of SiH_4 on a Si(001) surface. The results have been published in Ref. [2].

We consider the adsorption of SiH_4:

$$SiH_{4(g)} \rightarrow SiH_{3(ads)} + H_{(ads)}$$
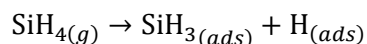
and the $SiH_{3(ads)}$ decomposition following the reaction:

$$SiH_{3(ads)} \rightarrow SiH_{2(ads)} + H_{(ads)}$$
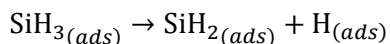
The SiH_4 adsorption is studied on a non-hydrogenated surface (θ = 0 ML) or a surface with a monolayer H coverage except for two Si atoms (θ = 1−2/16 = 0.875 ML). In the case of the hydrogenated surface, $SiH_{3(ads)}$ and $H_{(ads)}$ are adsorbed on the two unpassivated Si atoms.

The dissociative adsorption reaction of SiH_4 on the Si(001) surface can follow different pathways [3]: the intra-dimer, the inter-dimer, and inter-row mechanisms. In this work, we investigate the inter-dimer adsorption of silane.

All the calculations were done at the PBE+D3 level with an energy cutoff of 250 eV for the plane-wave basis and a 2x2x1 k-mesh. Geometric optimizations were performed by minimizing the forces of all atoms to 10 meV/Å. Finally, the energy barriers involved in the different reactions were computed using the Climbing Image Nudged Elastic Band method (CI-NEB).

2.2.1 SiH_4 adsorption without H coverage

The different configurations of the adsorption reaction corresponding to initial state (IS), intermediate states and final state (FS) are shown in Figure 2. The calculated energy diagram including the transition states (TS) is shown in Figure 3. We considered two different pathways for the dissociation of $SiH_{3(ads)}$ and corresponding to two different positions of $SiH_{2(ads)}$: either bounded to two Si atoms of two neighboring dimers from different rows (path a) or to two Si atoms of a same dimer (path b).
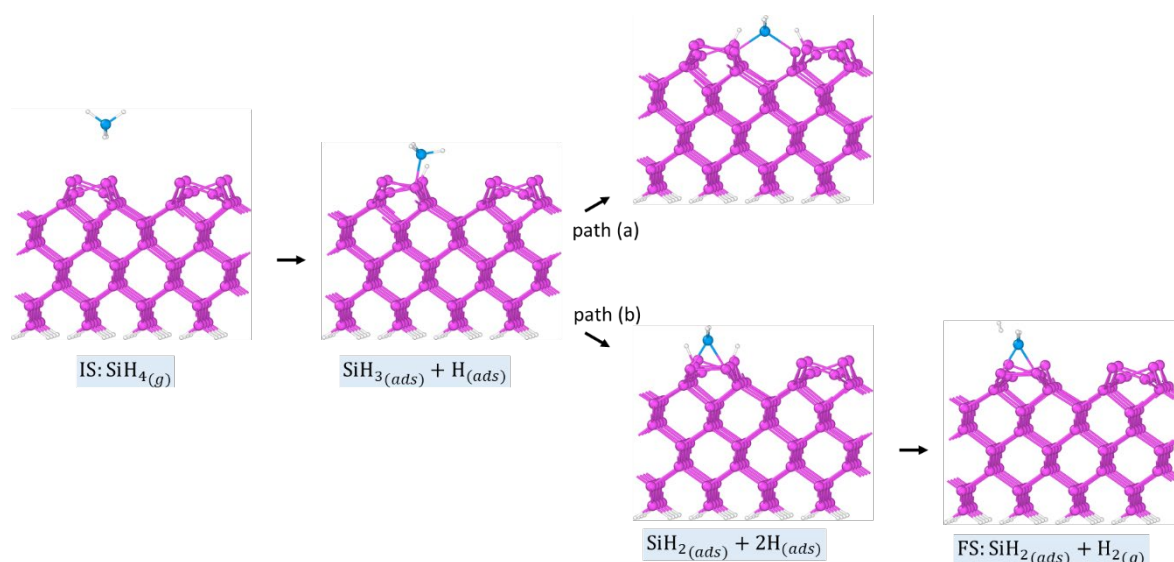
Figure 2: Relaxed configurations during the dissociative adsorption reaction of SiH₄ without H coverage. H and Si atoms are represented in white and purple, respectively. The Si atom involved in the adsorption reaction is shown in blue.

Figure 3: Reaction path energies of SiH₄ adsorption on two dimers of Si(001) surface without hydrogen coverage. The asterisk denotes adsorbed species.

Our simulations show that the adsorption reaction is exothermic and energetically favorable: the calculated reaction energy is -2.25 eV to adsorb SiH_2 from a chemisorbed SiH_4 (path b). The reaction is then dominated by the desorption of H atoms (adsorbed on neighboring dimers):

$$H_{(ads)} + H_{(ads)} \rightarrow H_{2(g)}$$
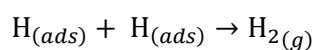
The corresponding activation and reaction energies are 2.4 eV and 1.92 eV, respectively, in good agreement with previous theoretical works [4]. H_2 desorption is energetically not favorable and kinetically limited but the whole adsorption process from remains

thermodynamically favorable. It should be noted that in Ref. [8], additional dissociative reactions have been studied and the authors found that $SiH_{(ads)}$ is the most stable adsorbate.

2.2.2 SiH$_4$ adsorption with H coverage

The different configurations of the adsorption reaction corresponding to the IS, intermediate state, and FS are shown in Figure 4. The calculated energy diagram including the TS is shown in Figure 5.

IS: $SiH_{4(g)}$　　　　　$SiH_{3(ads)} + H_{(ads)}$　　　　　$SiH_{2(ads)} + 2H_{(ads)}$

Figure 4: Relaxed configurations during the dissociative adsorption reaction of SiH$_4$ with H coverage. H and Si atoms are represented in white and purple, respectively. The Si atom involved in the adsorption reaction is shown in blue.
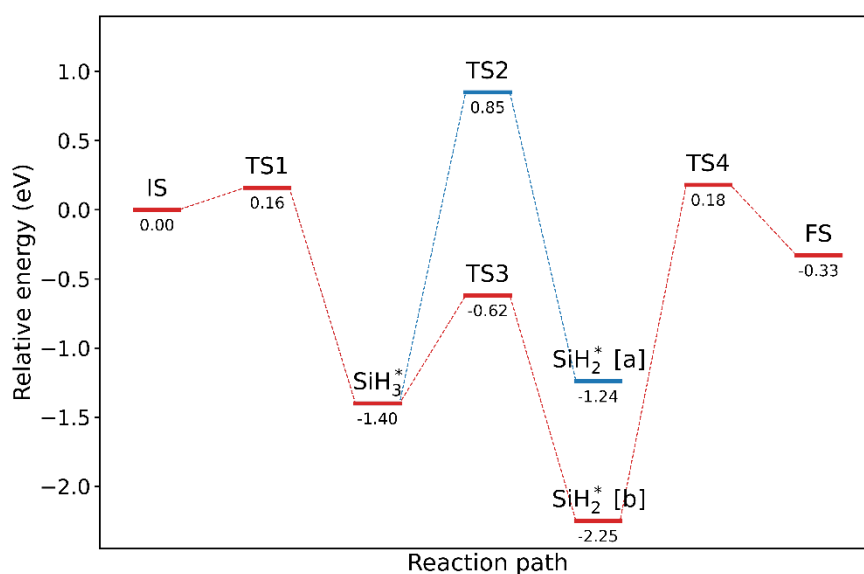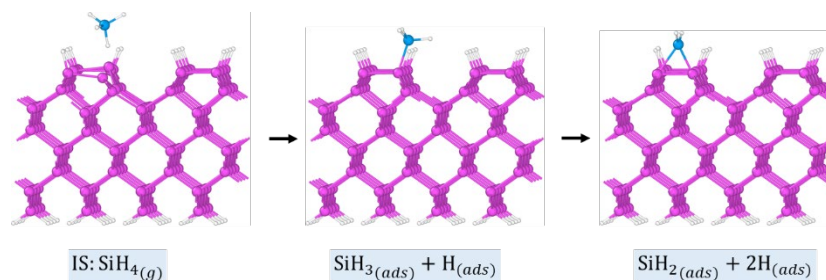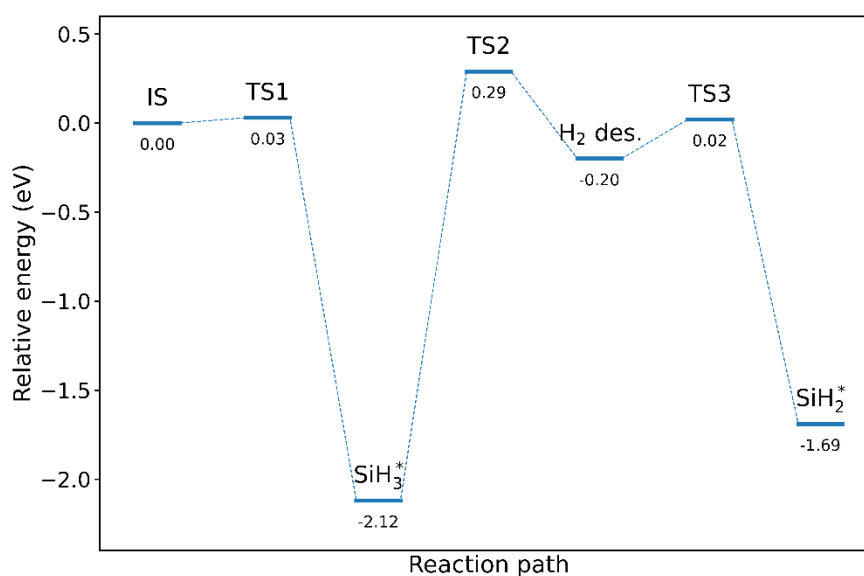

Figure 5: Reaction path energies of SiH$_4$ adsorption on two dimers of Si(001) surface with hydrogen coverage. The asterisk denotes adsorbed species.

As for the silane adsorption on a Si(001) surface without H coverage, we find that the reaction is exothermic and energetically favorable but with a smaller reaction energy of -1.69 eV. Interestingly, the adsorbed SiH$_3$ is the most stable configuration (more stable than adsorbed SiH$_2$). The kinetics is again limited by H$_2$ desorption (with an activation energy of ~2.4 eV) while there is almost no activation energy barrier for SiH$_3$ and SiH$_2$ adsorption.

Our calculations suggest that the description of H reactions at the Si surface plays an important role in the kinetics of silane adsorption. Therefore, an accurate description of H coverage will be central for the calibration of epitaxial growth LKMC models.

2.3 Silicon etching

In the previous section we have described the steps of the addition of a Si atom to a Si(001) surface, the smallest building block of epitaxial growth. Here, we consider the reverse process: the Si etching. Experimentally, the different existing recipes share the presence of HCl in the reaction chamber, yet a detailed atomistic description of the reaction mechanism has not been addressed yet. We studied the possible reaction paths using DFT simulations, computed their reaction energy profiles, and investigated the impact of Cl_2, another possible reactant for Si etching. We focused on the non-passivated and fully-passivated Si(001) surfaces, and considered the adsorbed SiH_2 as the reactant to etch. The results of this work will be reported in a separate paper [5].

3. Calibration and simulations of epitaxial growth using Synopsys Sentaurus

Within this chapter Sentaurus Process from the Synopsys Sentaurus TCAD software suite is used to simulate the epitaxial growth of SiGe thin films on a Si surface. For all simulations within this chapter, the LKMC module for epitaxial growth from Sentaurus Process is used together with AdvancedCalibration KMC from version U-2022.12 [6, 7]. We demonstrate our results for both undoped epitaxy and *in situ* doped epitaxy. The final simulations are based on recipes from CEA that are similar to the XLAST prototype. These recipes use the following precursors: H_2 as a carrier gas, dichlorosilane (DCS) and germane for the non-doped epitaxy, and in addition HCl and diborane for *in situ* doped epitaxy. In the following, we will first describe the model used for the LKMC epitaxy simulations, and then discuss the calibration of the individual precursors based on experimental data from literature. Finally, we demonstrate the final calibrations by simulating the recipes from CEA.

3.1 Model for LKMC simulations

Several models are available within Sentaurus Process KMC to simulate epitaxial growth. We use the most complex one, called `Coordinations.Reactions`, which is based on atomic bonding. For a more in-detail description of the models we refer to the Sentaurus Process user guide [6, 7]. The model is set up as a series of chemical reactions, occurring at the surface. Note that gas-phase reactions are not included within the model. The reaction rates for the different reactions are modelled as Arrhenius laws,

$$R = A \cdot e^{-E/k_B T},$$

where A is the reaction prefactor that can be tuned during calibration, and E is the activation energy for the reaction given by

$$E = E_0 + f_r \sum_r E_r(c) + f_p \sum_p E_p(c).$$

Here E_0 is a basic energy that can be tuned during calibration, r and p denote the different reactants and products, respectively, $f_{r/p}$ are the reactant- and product prefactors and $E_{r/p}(c)$ are the coordination dependent formation energies. Note that contributions from atoms up to the third-nearest neighbors are included within the model.

The different reactions are grouped into the following categories:

- Adsorption reactions: the reaction prefactor is given by $A = r_0 J_i$, where r_0 is tunable during calibration, and $J_i \sim P_i / \sqrt{m_i T}$ is the species dependent arrival rate, with P_i being the species' partial pressure, m_i the mass of the gas molecule of the precursor, and T the temperature. No reactants are involved during adsorption reactions.
- Surface reactions: the reaction prefactor is given by $A = r_0$. Both, products and reactants are involved during surface reactions.
- Desorption reactions: the reaction prefactor is given by $A = r_0$. No products are involved during desorption reactions.
- Etching reactions: the reaction prefactor is given by $A = r_0 J_i$, as for adsorption reactions. No products are involved in etching reactions.
- Surface segregation: two-site exchange reactions, where the participating species exchange their sites.

In addition, surface diffusion is enabled during the LKMC simulations. Usually, surface diffusion has no significant impact on growth rates or parameters like Ge content, but without it surfaces may become unrealistically rough.

There are two parameter sets implemented within Sentaurus Process AdvancedCalibration KMC, the standard one, and one that focuses on SiGe epitaxy. The latter is activated by calling the `LKMC_SiGe_Epitaxy` procedure. We are mostly working with the latter one but will point it out whenever it is activated.

3.2 Dichlorosilane

DCS (SiH_2Cl_2) is a popular precursor for Si epitaxial growth. The epitaxy is modeled via the following reactions, where * denotes a passivating species.

- Adsorption

$$SiCl_2H_2(g) \rightarrow SiH^*$$
$$SiCl_2H_2(g) \rightarrow H^*$$

- Surface

$$SiH^* \rightarrow Si$$
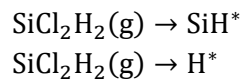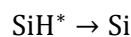
Since hydrogen is used as a carrier gas, hydrogen reactions are also relevant. They are given by

- Adsorption

$$H_2(g) \rightarrow H^*$$

- Desorption

$$H^* \rightarrow H_2(g)$$
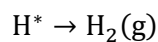
This means it is assumed that DCS decomposes into surface passivating products silylene and hydrogen, while the chlorine is supposed to desorb immediately. Silylene then decomposes into Si.

Figure 6: Growth rate as a function of DCS flow rate for different orientations of the substrate at an epitaxy temperature of (left) 750 °C and (right) 1050 °C. The pressure is 20 Torr. Experimental values are from Ref. [8].
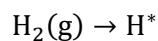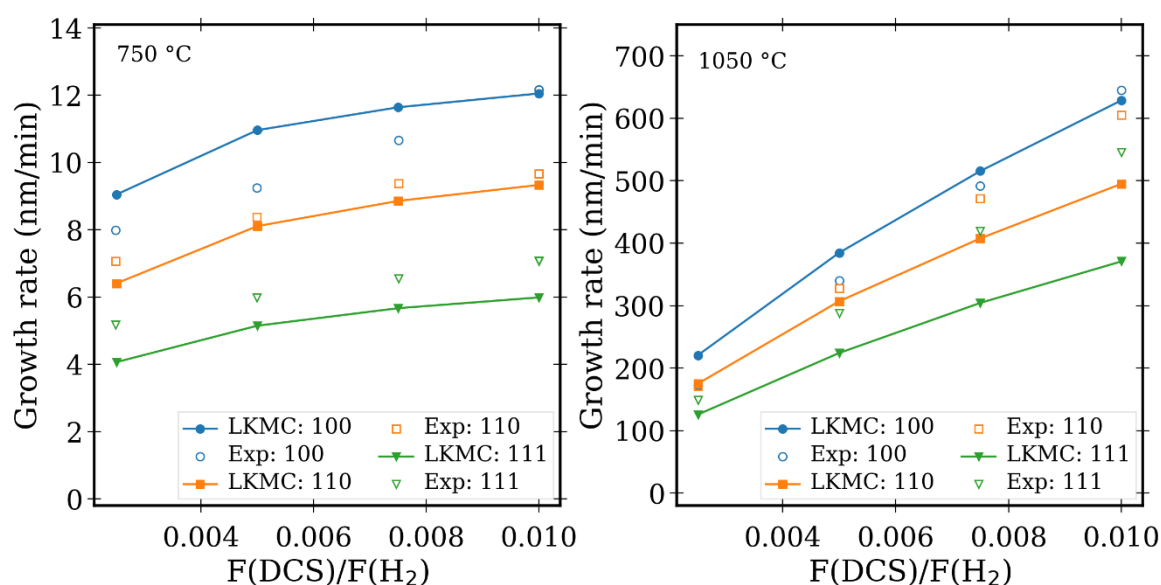
In Figure 6 we show results from LKMC simulations with AdvancedCalibration KMC, denoted by lines and full symbols, compared to results from experiment [8], denoted by empty symbols. Shown is the growth rate as a function of the DCS flow rate for different substrate orientations. For the case of 750 °C (left) simulations nicely reproduce the experiment. For (100) orientation simulation results slightly overestimate the growth rate, while for (111) they slightly underestimate it. At 1050 °C (right), we again find a good reproduction of experimental data, where for both the (110) and (111) direction the growth rate is underestimated. This becomes more severe for higher flow rates of DCS.

AdvancedCalibration KMC is able to reproduce experimental data rather well, especially for low temperatures. Within the MUNDFAB project low temperature processes are more relevant, and as a result an underestimation of the growth rate at high temperatures is not a big concern here. Therefore, we will keep the calibration for DCS and focus on germane and hydrogen chloride, which are more critical.

3.3　Germane

Germane (GeH_4) is usually used together with DCS and hydrogen as a carrier gas, for SiGe epitaxy. Since we are not aware of recipes published in the literature that include germane exclusively, we focus on the calibration of germane in recipes that contain both germane and DCS. As a result, the reactions from DCS are relevant here, too. In addition, the following reactions are used to model germane as a precursor.

- Adsorption

$$GeH_4(g) \rightarrow GeH_2{}^*$$
$$GeH_4(g) \rightarrow H^*$$
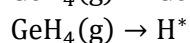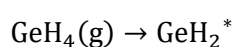
- Surface

$$GeH_2^* \rightarrow Ge$$
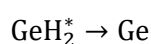
Finally, surface segregation is active for Si and Ge atoms. This means that the germane epitaxy is modeled by decomposition into the surface passivating products germylene and hydrogen. Germylene then decomposes into Ge via a surface reaction. Just as before, hydrogen is used as carrier gas.

We activate `LKMC_SiGe_Epitaxy` for SiGe epitaxy. In Figure 7 and Figure 8 we show results for the AdvancedCalibration KMC in comparison with data from Refs. [8, 9].

Figure 7: (left) Growth rate as a function of germane flow rate for different substrate orientations. (right) Ge content as a function of germane flow rate for different substrate orientations. The pressure was 20 Torr, the DCS flowrate is given by F(DCS) = 0.01 F(H₂), and epitaxy temperature is 700 °C. Experimental values are from Ref. [8].

From Figure 7 two main issues of the AdvancedCalibration KMC of SiGe epitaxy based on DCS and germane become obvious: For one, the grow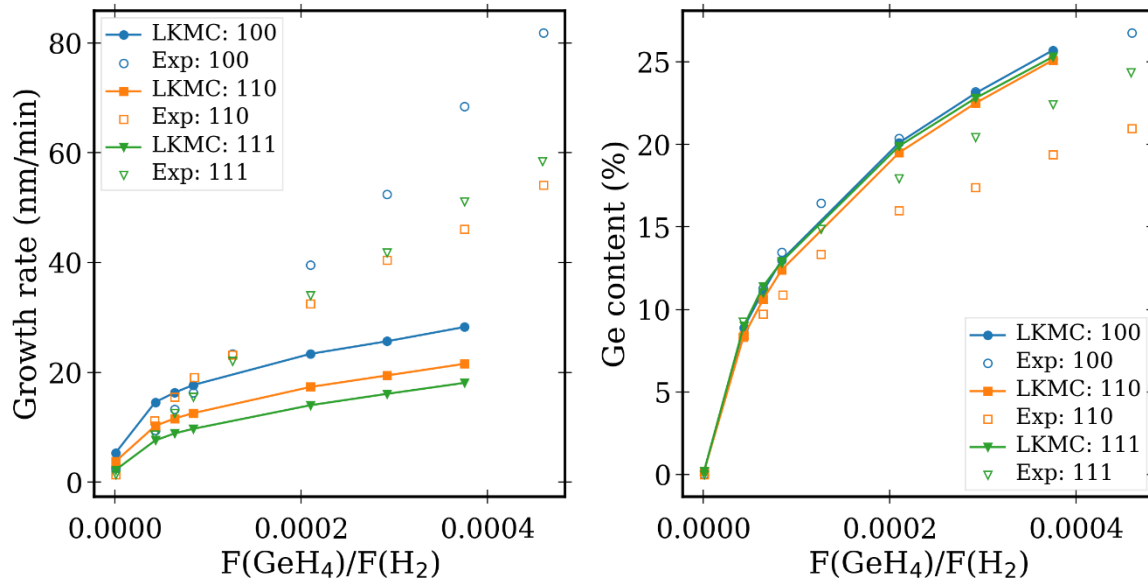th rate is severely underestimated for intermediate to high germane flow rates and fits are only reasonable at flow rates $F(\mathrm{GeH_4}) < 0.0001\, F(\mathrm{H_2})$. This is especially problematic since we are mostly interested in flow rates $F(\mathrm{GeH_4}) > 0.0001\, F(\mathrm{H_2})$. On the other hand, for (100) substrate, the Ge content is well reproduced, but the impact of changing the orientation is underestimated. The first problem is also visible in Figure 8, where on the left the growth rate is plotted as a function for germane flow at different temperatures. We see the same problem of underestimating the growth rate for medium to high germane flows. On the right the Ge content is plotted as a function of germane flow, again for different temperatures. Here we find a good reproduction of the Ge content at lower temperatures, while for 650 and 700 °C the Ge content is overestimated. We emphasize that in both figures experiments show that at high temperatures the growth rate as a function of germane flow rate is almost linear, which is not reproduced in simulation.
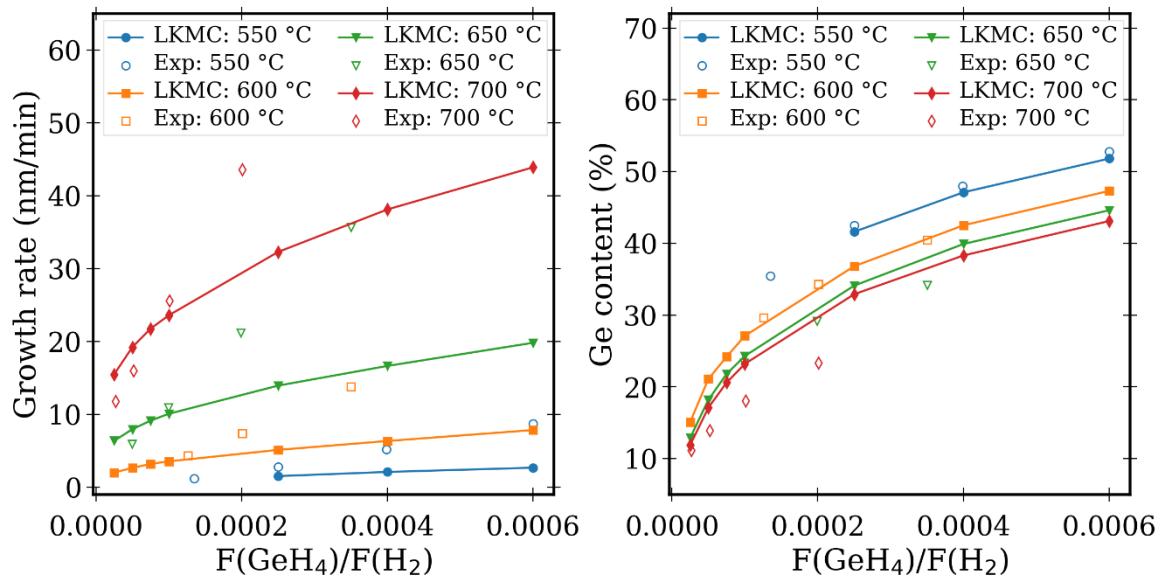
Figure 8: (left) Growth rate as a function of germane flow rate for different substrate orientations. (right) Ge as a function of germane flow rate for different substrate orientations. The pressure was 20 Torr, the DCS flowrate is given by F(DCS) = 0.003 F(H₂), the substrate orientation is (100). Experimental values are from Ref. [9].

Since we found that the DCS simulations were sufficient, we limit our calibration to the three germane-specific reactions, defined above. In addition, we also tune the energy and prefactor for Si-Ge surface segregation. We did not find a way to perfectly fit the experimental data from literature, especially the almost linear behavior of the growth rate and the underestimate of the impact of substrate orientation are not well reproduced. As a result, we focus on parameters that are relevant for the recipes, discussed within MUNDFAB, especially those discussed in Section 3.5. This means, we focus especially on good fits for intermediate germane flow rate of about $F(\mathrm{GeH_4})/F(\mathrm{H_2}) \sim 1.5 \times 10^{-4}$.

In Table 1 we show the changed set of parameters in comparison to AdvancedCalibration KMC with `LKMC_SiGe_Epitaxy`. We decrease the energy barrier for the silicon-germanium surface segregation while increasing the respective prefactor to increase the surface segregation effect. This increases the growth rate while decreasing the Ge content. We note, that when trying to fit higher germane flow rates, it is necessary to also decrease the energy barrier for germane adsorption, to further increase the growth rate and the Ge content, and then stronger increase the effect of surface segregation.

Table 1: Final calibration of Germane-relevant parameters that were changed from their standard values in AdvancedCalibration KMC.

Si-Ge surface segregation barrier	0.05 eV
Si-Ge surface segregation prefactor	24.7

We reproduce Figure 7 and Figure 8 but with this additional calibration in Figure 9 and Figure 10, respectively. The case of different substrate orientations (Figure 9) is still not very well reproduced. The difference in the Ge content for the substrate orientations is slightly increased compared to the AdvancedCalibration KMC results. For the (111) and (110) substrate orientation we find good fits, except for high flow rates where the Ge content is overestimated

for (110). The (100) orientation is slightly underestimated throughout, but the differences are small, and the general form is well reproduced. The growth rate is increased and fits the experimental data at the desired, intermediate germane flow rather well. However, we still find that the (111) orientation has a lower growth rate than (110), which is the other way around in the experiment.
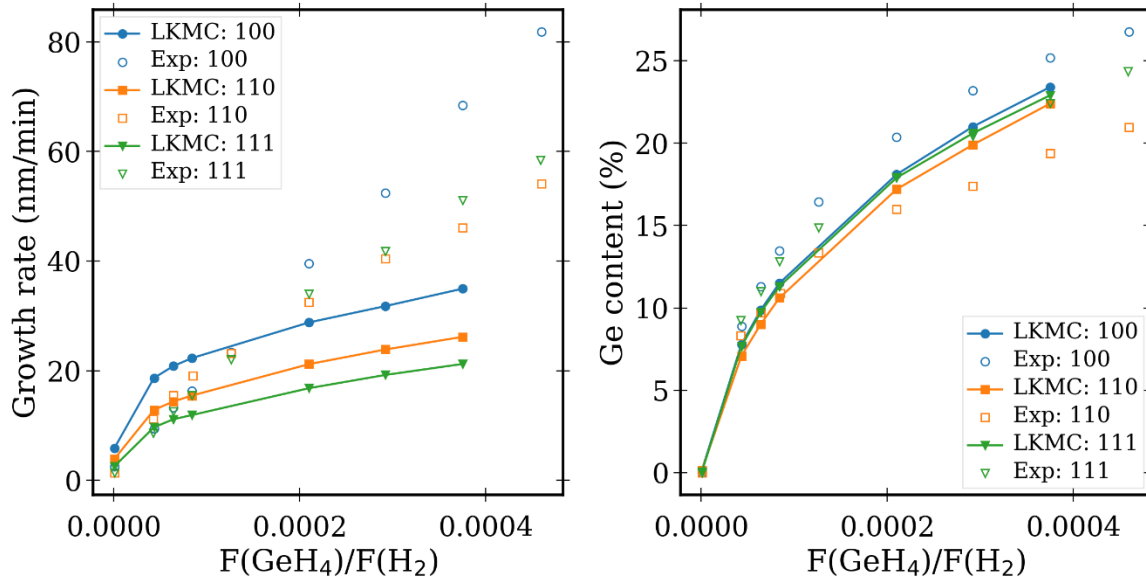
Figure 9: Same as Figure 7 but with the additional calibration from Table 1.
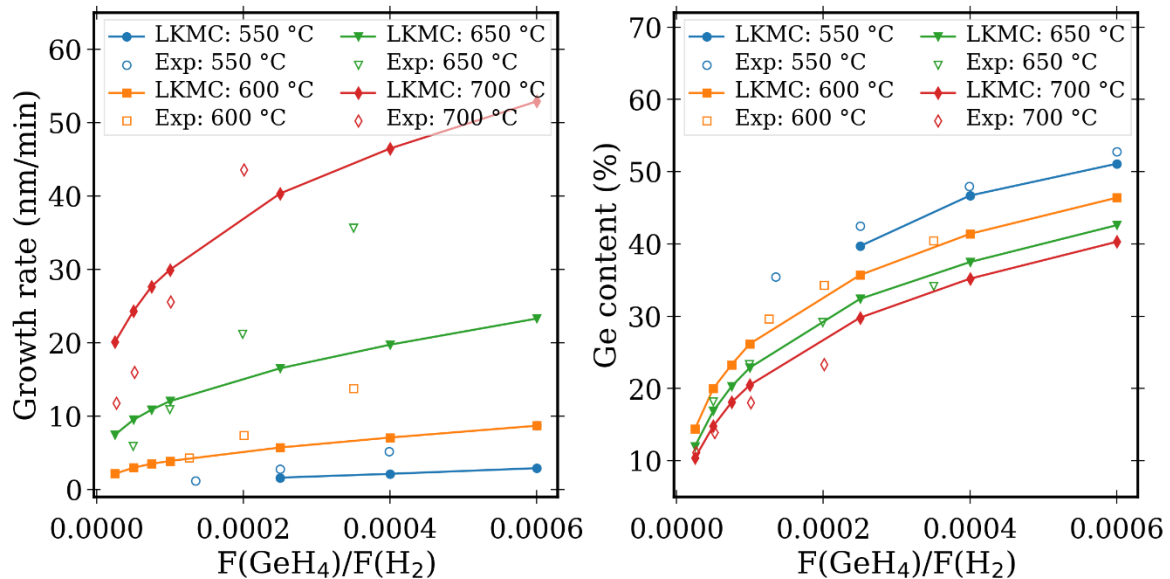
Figure 10: Same as Figure 8 but with the additional calibration from Table 1.

Looking at different temperatures, we find that the growth rate is significantly increased, leading to good fits at intermediate germane flow rates, even though the general form of the curves is not reproduced (at low germane flow rates the growth rate is overestimated, at high flow rates it is underestimated) since the experimental data shows the mostly linear behavior, that was already discussed before. The fits to the Ge content, however, are improved in comparison to AdvancedCalibration KMC. For temperatures of 550 °C - 650 °C, we find almost

perfect fits to the experimental data. Only for the case of 700 °C the simulation slightly overestimates the Ge content, but the difference is only a few percent and significantly lower, as what we have found with AdvancedCalibration KMC.

3.4 Hydrogen Chloride

Hydrochloric acid (HCl) is added as a precursor for the selective epitaxial growth of Si or SiGe high-quality layers inside oxide windows, making it useful for the formation of raised sources and drains [10], [11]. HCl is an etchant for Si, SiGe and Ge, but it does not etch SiO_2 [12]. The HCl etching is modeled in Sentaurus Process LKMC with the following reactions [6], [7]:

- Adsorption

$$HCl(g) \rightarrow H^*$$
$$HCl(g) \rightarrow Cl^*$$

- Surface

$$Si + Cl^* \rightarrow SiCl_2^*$$
$$Ge + Cl^* \rightarrow GeCl_2^*$$

- Desorption

$$SiCl_2^* \rightarrow SiCl_2(g)$$
$$GeCl_2^* \rightarrow GeCl_2(g)$$
$$H^* \rightarrow H_2(g)$$
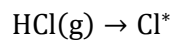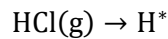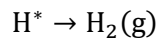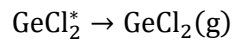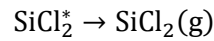
Also, for the simulations of the HCl etching of SiGe, we activate `LKMC_SiGe_Epitaxy`. Firstly, we present the results of the simulations using default parameters from AdvancedCalibration KMC [7]. We notice that using the default parameters, the surface of the SiGe and Ge is not flat and regular for the temperature range that is of the most interest for this study, i.e. 60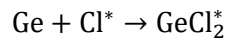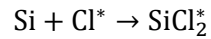0 °C – 700 °C. Figure 11, Figure 12 and Figure 13 show the surface of $Si_{0.67}Ge_{0.33}$, $Si_{0.5}Ge_{0.5}$ and Ge, respectively, resulting from LKMC simulations of HCl etching (substrates (001), HCl partial pressure of 0.208 Torr, total pressure of 20 Torr, hydrogen as carrier gas) for different temperatures. Results of $Si_{0.67}Ge_{0.33}$ (Figure 11) and $Si_{0.5}Ge_{0.5}$ (Figure 12) are for temperatures of 650 °C, 675 °C and 700 °C, whereas results of Ge (Figure 13) are for temperatures of 450 °C and 500 °C (the etching rate on pure Ge is much higher, so to obtain similar etching rate we decrease the temperature in this case).
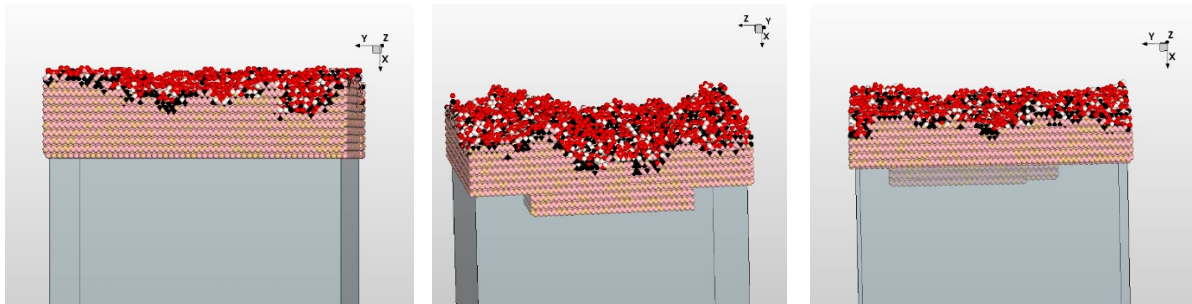
Figure 11: Sentaurus Process LKMC simulation results, using default parameters from AdvancedCalibration, of HCl etching of $Si_{0.67}Ge_{0.33}$ (substrates (001), HCl partial pressure of 0.208 Torr, total pressure of 20 Torr, hydrogen as carrier gas) for different temperatures: (left) 650 °C, (middle) 675 °C, (right) 700 °C. Red spheres represent H*, pink spheres represent Si, beige spheres represent Ge, black spheres represent $SiCl_2^*$ and $GeCl_2^*$, white spheres represent the non-passivated surface sites.
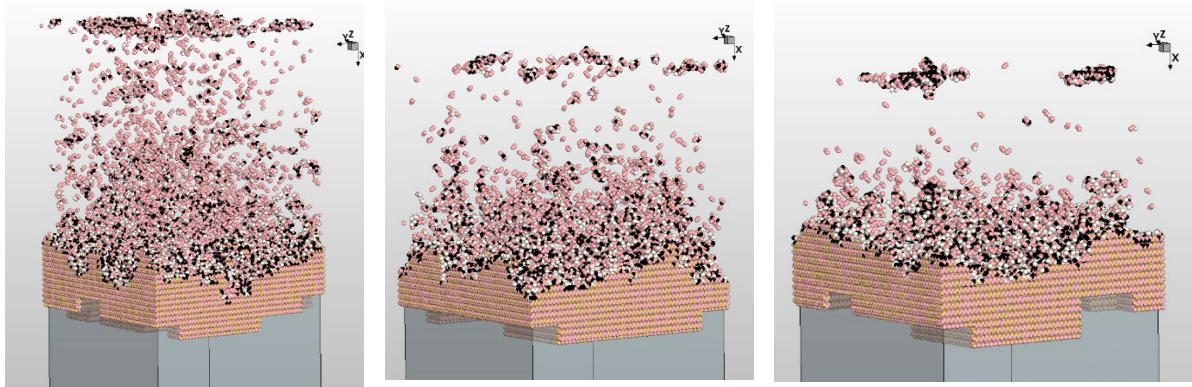
Figure 12: Same as Figure 11 but for HCl etching of Si$_{0.5}$Ge$_{0.5}$.
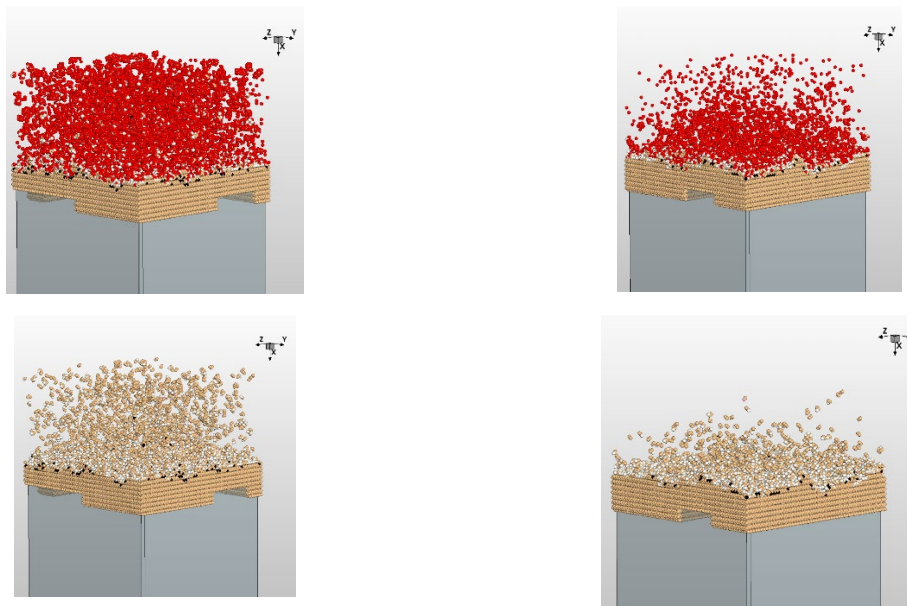
Figure 13: Sentaurus Process LKMC simulation results, using default parameters from AdvancedCalibration, of HCl etching of Ge (HCl partial pressure of 0.208 Torr, total pressure of 20 Torr, hydrogen as carrier gas) for different temperatures: (left) 450 °C, (right) 500 °C, (top) with and (bottom) without visualization of H* (red spheres). Beige spheres represent Ge, black spheres represent $SiCl_2^*$ and $GeCl_2^*$, white spheres represent the non-passivated surface sites.

As can be seen in Figure 11, the simulation of HCl etching of Si$_{0.67}$Ge$_{0.33}$ gives as results very rough surfaces, with deep valleys. The simulations of Si$_{0.5}$Ge$_{0.5}$ and Ge present an even bigger issue, as floating atoms in the gas, not attached to the substrate, appear (Figure 12). The first objective of the calibration work regarding HCl etching is thus to obtain a smooth surface without floating atoms. As the floating atoms are not found in simulations of HCl etching of silicon, first of all the prefactors and energies (*A* and *E$_0$* as explained above in this section) for the $GeCl_2^*$-specific reactions ($Ge + Cl^* \rightarrow GeCl_2^*$ and $GeCl_2^* \rightarrow GeCl_2(g)$) were set to the same values as the corresponding $SiCl_2^*$ reactions ($Si + Cl^* \rightarrow SiCl_2^*$ and $SiCl_2^* \rightarrow SiCl_2(g)$). The simulation results, using this new set of parameters (`calib_HCl_v1`), are shown in Figure 14, Figure 15 and Figure 16.
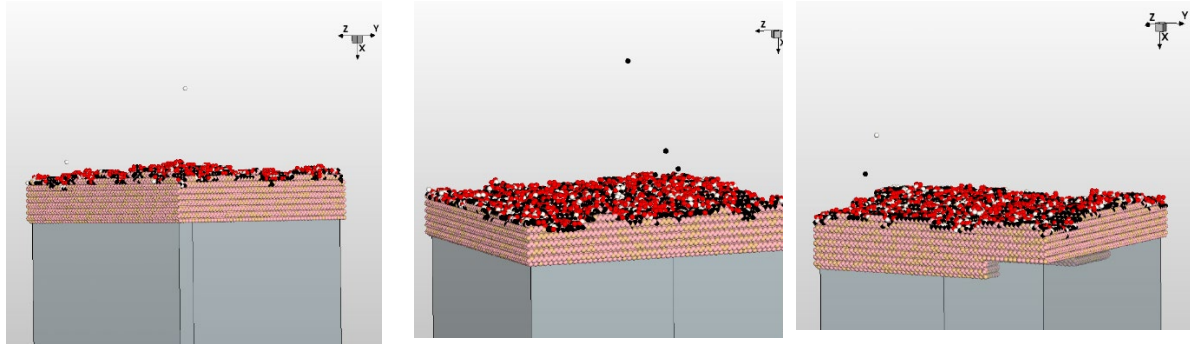
Figure 14: Sentaurus Process LKMC simulation results, using modified parameters (`calib_HCl_v1` set), of HCl etching of Si0.67Ge0.33 (substrates (001), HCl partial pressure of 0.208 Torr, total pressure of 20 Torr, hydrogen as carrier gas) for different temperatures: (left) 650 °C, (middle) 675 °C, (right) 700 °C. Red spheres represent H^*, pink spheres represent Si, beige spheres represent Ge, black spheres represent $SiCl_2^*$ and $GeCl_2^*$, white spheres represent the non-passivated surface sites.
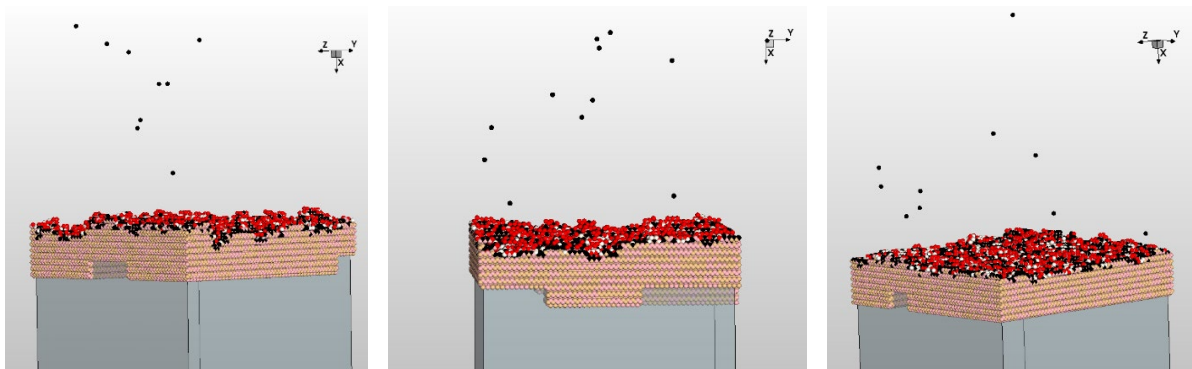
Figure 15: Same as Figure 14 but for HCl etching of Si0.5Ge0.5.
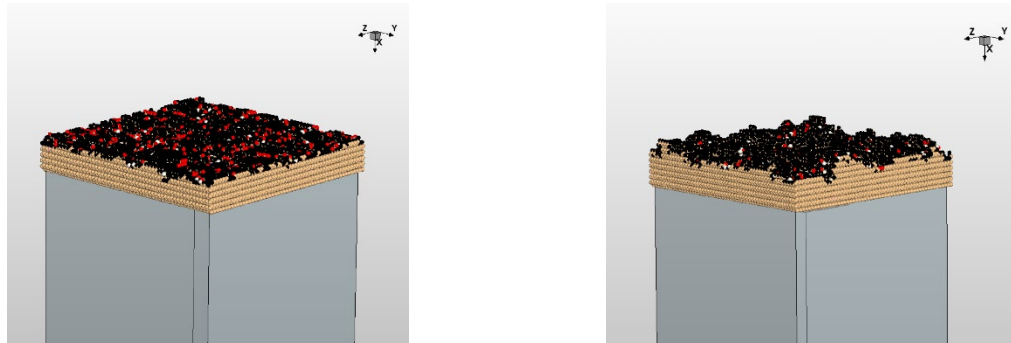
Figure 16: Sentaurus Process LKMC simulation results, using modified parameters (`calib_HCl_v1` set) of HCl etching of Ge (HCl partial pressure of 0.208 Torr, total pressure of 20 Torr, hydrogen as carrier gas) for different temperatures: (left) 450 °C, (right) 500 °C. Red spheres represents H, beige spheres represent Ge, black spheres represent $SiCl_2^*$ and $GeCl_2^*$, white spheres represent the non-passivated surface sites.*

With this set of parameters, smooth, regular, and planar surfaces are obtained in all cases. The floating atoms are not appearing in the structures (except for very few negligible passivating species). However, the use of this set of parameters also results in a decreased etch rate. The etch rate as a function of temperatures for $Si_{0.67}Ge_{0.33}$, $Si_{0.5}Ge_{0.5}$ and Ge (HCl partial pressure of 0.208 Torr, total pressure of 20 Torr) and as a function of HCl partial pressure (temperature of 700 °C) using AdvancedCalibration default parameters is shown in Figure 17. The etch rate as a function of temperature and as a function of partial pressure using the parameters `calib_HCl_v1` is shown in Figure 18. The simulated etch rates are compared against published experimental data [12], plotted with empty symbols.
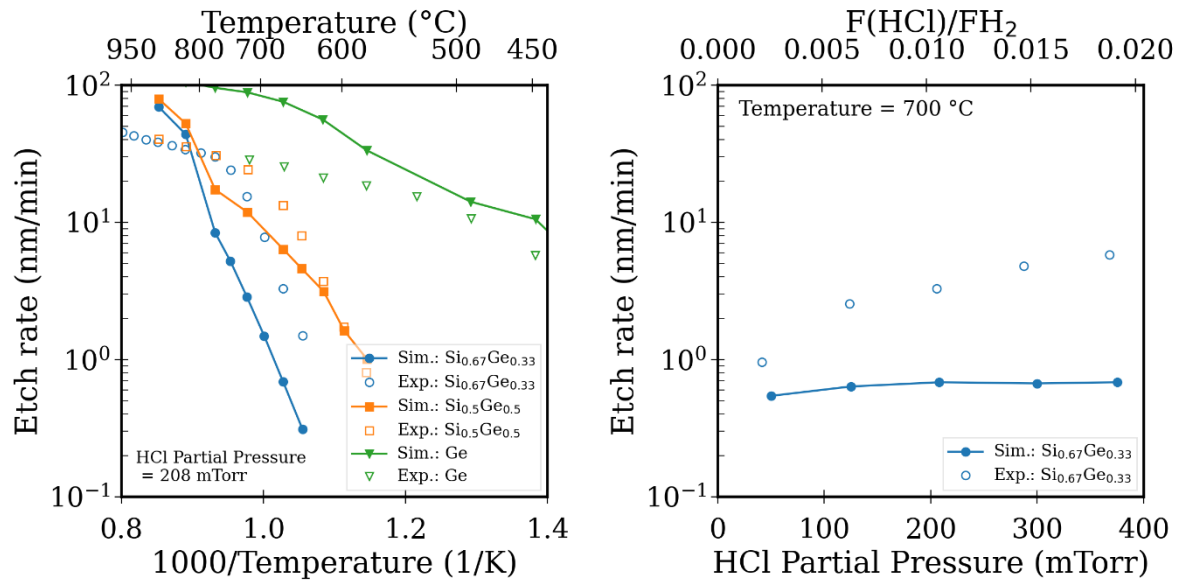
Figure 17: Simulated etch rate as a function of temperatures for $Si_{0.67}Ge_{0.33}$, $Si_{0.5}Ge_{0.5}$ and Ge (HCl partial pressure of 0.208 Torr, total pressure of 20 Torr) and etch rate as a function of HCl partial pressure for $Si_{0.67}Ge_{0.33}$ (temperature of 700 °C) using AdvancedCalibration default parameters (solid lines and full symbols). Experimental data, from [12], are plotted with empty symbols.
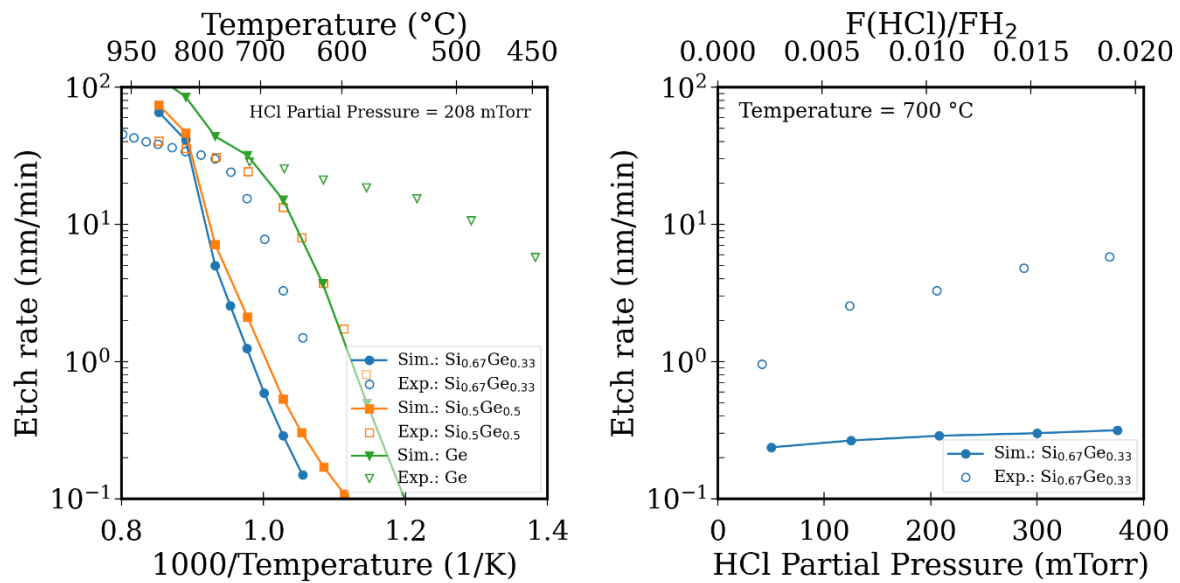
Figure 18: Simulated etch rate as a function of temperature for $Si_{0.67}Ge_{0.33}$, $Si_{0.5}Ge_{0.5}$ and Ge (HCl partial pressure of 0.208 Torr, total pressure of 20 Torr) and etch rate as a function of HCl partial pressure for Si0.67Ge0.33 (temperature of 700 °C) using parameters set `calib_HCl_v1` (solid lines and full symbols). Experimental data, from [12], are plotted with empty symbols.

Figure 19 reports two examples of the simulated etched thickness as a function of time (700 °C and HCl partial pressure of 50 mTorr) for the AdvancedCalibration KMC and `calib_HCl_v1` parameter sets. The etch rate is computed considering etched thickness above 1 nm.
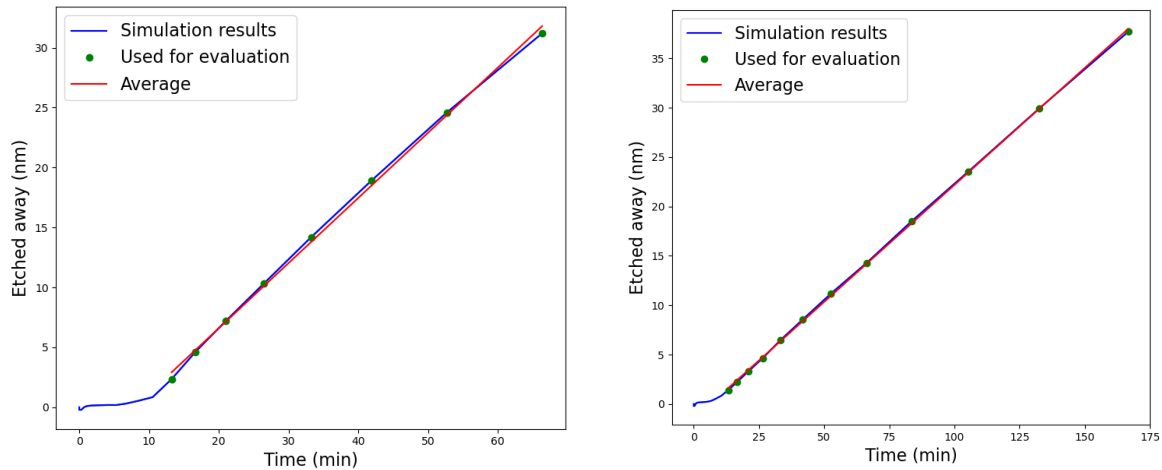
Figure 19: Simulated etched thickness as a function of time (700 °C and HCl partial pressure 50 mTorr) for (left) AdvancedCalibration default parameters and (right) set `calib_HCl_v1`. The etch rate is calculated considering the green points, i.e., starting from an etch thickness of 1 nm.

As stated before, with parameters in `calib_HCl_v1` set, the simulated surfaces are correct, but the etch rate is too low. For this reason, calibration work was performed to obtain a better fit for the etch rate, without degrading the surface or obtaining floating atoms. The simulation of HCl etching of Si performed in Sentaurus Process LKMC with default AdvancedCalibration KMC parameters provide good results in the temperature range of interest, as shown in Figure 20. It can be inferred that the parameters for the Ge-specific reactions need to be adjusted. The calibration work thus focused on the prefactors and energies of the reactions $Ge + Cl^* \rightarrow GeCl_2^*$ (from now on referred as HCl_Ge_etch) and $GeCl_2^* \rightarrow GeCl_2(g)$ (from now on referred as GeCl2_des).
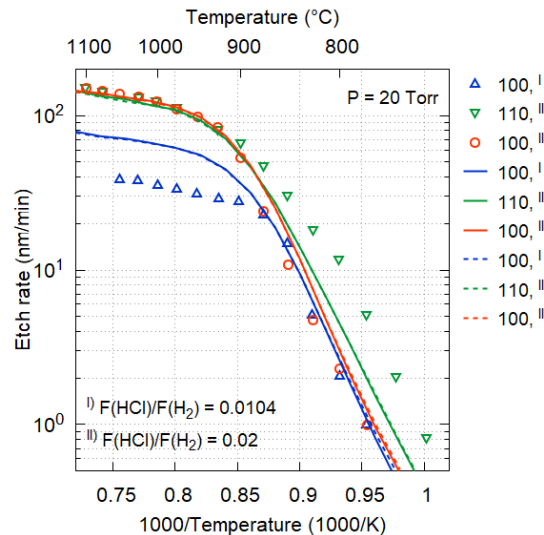
Figure 20: Simulated etch rate as a function of temperatures of HCl on Si, using AdvancedCalibration KMC default parameters (solid lines). Experimental data, from [12], [13], are plotted with empty symbols.

Varying the energies and prefactors (E_0 and A) of HCl_Ge_etch and GeCl2_des is possible to increase the etch rate, with respect to what is shown in Figure 18. However, a significant increase in the etch rate, to match the experimental data, results also in floating atoms, even

with significantly different parameters from the default ones. Table 2 reports in green the combinations of E_0 and A of GeCl2_des which result in planar surfaces and in red the combinations resulting in floating atoms. E_0 and A refer only to GeCl2_des because changing E_0 and A of HCl_Ge_etch in the range between AdvancedCalibration default values and `calib_HCl_v1` values resulted in a negligible change of etch rate (for Ge) or further decrease of etch rate (for $Si_{0.67}Ge_{0.33}$ or $Si_{0.5}Ge_{0.5}$) and the same type of surface. Increasing E_0 of HCl_Ge_etch to higher values, i.e., outside the range, up to 3.6 eV, is possible to increase the etch rate, but floating atoms appear, so this situation is not taken into consideration. In Table 2, E_0 and A of HCl_Ge_etch are kept as in the `calib_HCl_v1` parameter set. Table 2 shows results separately for the case of Ge, $Si_{0.67}Ge_{0.33}$ or $Si_{0.5}Ge_{0.5}$, as floating atoms appear for different conditions.

Table 2: Combinations of energies and prefactors (E_0 and A) of GeCl2_des reaction resulting in correct surfaces (green) or surfaces with floating atoms (red). Yellow refers to a surface without floating atoms or a very rough shape, that is not as good as the cases labeled green. E_0 and A of HCl_Ge_etch reaction are kept as in `calib_HCl_v1.`

Ge					
	E_0				
A	1	1.3	1.5	1.7	2
$1.00 \cdot 10^{30}$	red	green	green	green	green
$1.00 \cdot 10^{32}$	red	red	green	green	green
$1.00 \cdot 10^{33}$	red	red	red	green	green
$1.00 \cdot 10^{34}$	red	red	red	red	green

$Si_{0.5}Ge_{0.5}$					
	E_0				
A	1.7	2	2.5	3	3.5
$1.00 \cdot 10^{30}$	red	red	green	green	green
$1.00 \cdot 10^{32}$	red	red	red	green	green
$1.00 \cdot 10^{33}$	red	red	red	red	green
$1.00 \cdot 10^{34}$	red	red	red	red	green

$Si_{0.67}Ge_{0.33}$					
	E_0				
A	1.5	1.7	2.3	2.5	2.7
$1.00 \cdot 10^{28}$	green	green	green	green	green
$1.00 \cdot 10^{30}$	yellow	yellow	green	green	green
$1.00 \cdot 10^{32}$	red	red	red	green	green
$1.00 \cdot 10^{40}$	red	red	red	red	green

For the case of $Si_{0.67}Ge_{0.33}$, the yellow entries refer to a surface without floating atoms or a very rough shape, however still not as good as the other surfaces indicated in green. Decreasing E_0, the etch rate increases, whereas decreasing A, the etch rate decreases. So, the best parameters are selected identifying the combination of lowest E_0 and highest A in the green part of the tables. So, for the GeCl2_des reaction, $A = 1.00 \cdot 10^{30}$ and E_0 =2.3 eV were obtained. The etch rate as a function of temperature and as a function of partial pressure using these calibrated parameters (`calib_HCl_v2`, summarized in Table 3) is shown in Figure 21.

Table 3: Calibrated parameters for selected reactions (`calib_HCl_v2`).

Reaction	Prefactor (A)	Energy (E_0)
$GeCl_2^* \rightarrow GeCl_2(g)$	$1.00 \cdot 10^{30}$	2.3
$Ge + Cl^* \rightarrow GeCl_2^*$	default value of $SiCl_2^* \rightarrow SiCl_2(g)$	default value of $SiCl_2^* \rightarrow SiCl_2(g)$

The main goal is to obtain the best parameters to be later used in the simulation of the full epitaxial recipes. Those recipes use a temperature of about 650 °C, with $F(HCl)/F(H_2)$ of 0.00183 corresponding to a HCl partial pressure of 36 mTorr targeting a Ge content of 33%. Experimental data of HCl etching with this temperature and pressure are not available, but 700 °C and low HCl partial pressure, the simulated etch rate with `calib_HCl_v2` parameter set is in rather good agreement with the measured etch rate. So, for the full epitaxial recipes the `calib_HCl_v2` will be used.

Figure 21: Simulated etch rate as a function of temperatures for $Si_{0.67}Ge_{0.33}$, $Si_{0.5}Ge_{0.5}$ and Ge (HCl partial pressure of 0.208 Torr, total pressure of 20 Torr) and etch rate as a function of HCl partial pressure for $Si_{0.67}Ge_{0.33}$ (temperature of 700 °C) using parameters set `calib_HCl_v2` (solid lines and full symbols). Experimental data, from [12], are plotted with empty symbols.

However, for higher HCl partial pressures, the etch rate is still too low, so to fit these data further calibration work is needed. Since HCl_Ge_etch parameters calibration to obtain higher etch rate results in floating atoms, as described above, an additional reaction was taken into consideration: the adsorption reaction $HCl(g) \rightarrow Cl^*$ (HCl_Cl_ads). As this reaction is not Ge-specific, its calibrated parameters must be used only when simulating HCl SiGe etching, while they should be kept equal to AdvancedCalibration default values when simulating HCl Si etching. Decreasing E_0 and increasing A, the etch rate increases. By decreasing E_0 down to 0 eV and increasing A up to 0.1, it is possible to increase the etch rate without degrading too much the flatness of the surface and without the presence of floating atoms. For pure Ge, E_0 = 0 eV and 0.05 eV in combination with $A > 0.002$ lead to $GeCl_2^*$ particles in the gas, but without the presence of Ge floating atoms. The best results in terms of flatness are obtained by varying only A. This set of calibrated parameters (`calib_HCl_v3`) is summarized in Table 4.

Table 4: Calibrated parameters for selected reactions (`calib_HCl_v3`).

Reaction	Prefactor (A)	Energy (E_0)
$GeCl_2^* \rightarrow GeCl_2(g)$	$1.00 \cdot 10^{30}$	2.3
$Ge + Cl^* \rightarrow GeCl_2^*$	default value of $SiCl_2^* \rightarrow SiCl_2(g)$	default value of $SiCl_2^* \rightarrow SiCl_2(g)$
$HCl(g) \rightarrow Cl^*$	$2.00 \cdot 10^{-3}$	default value

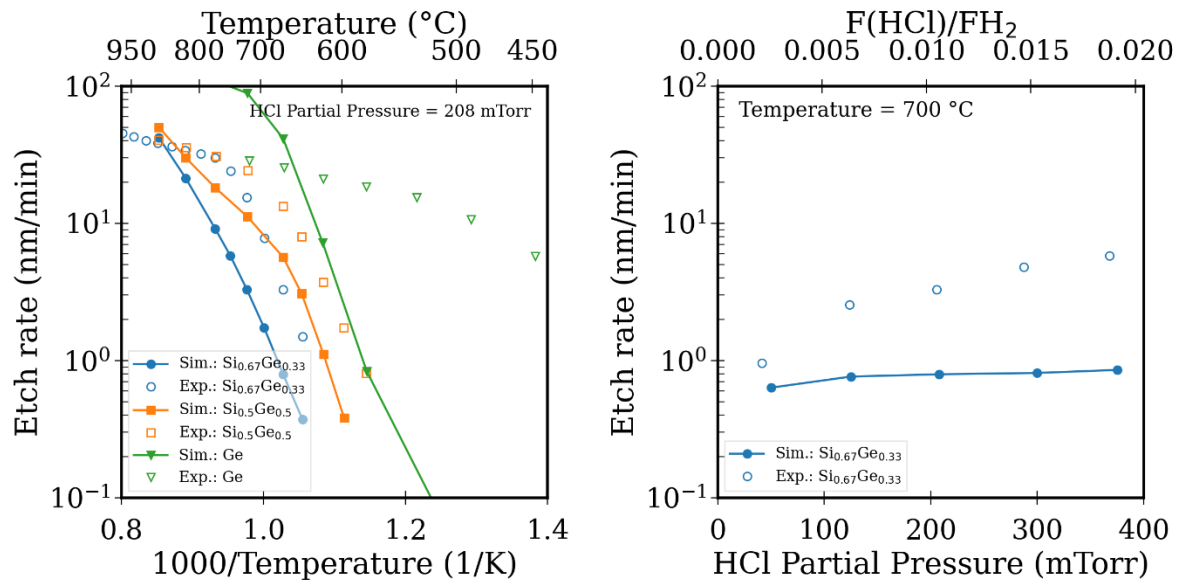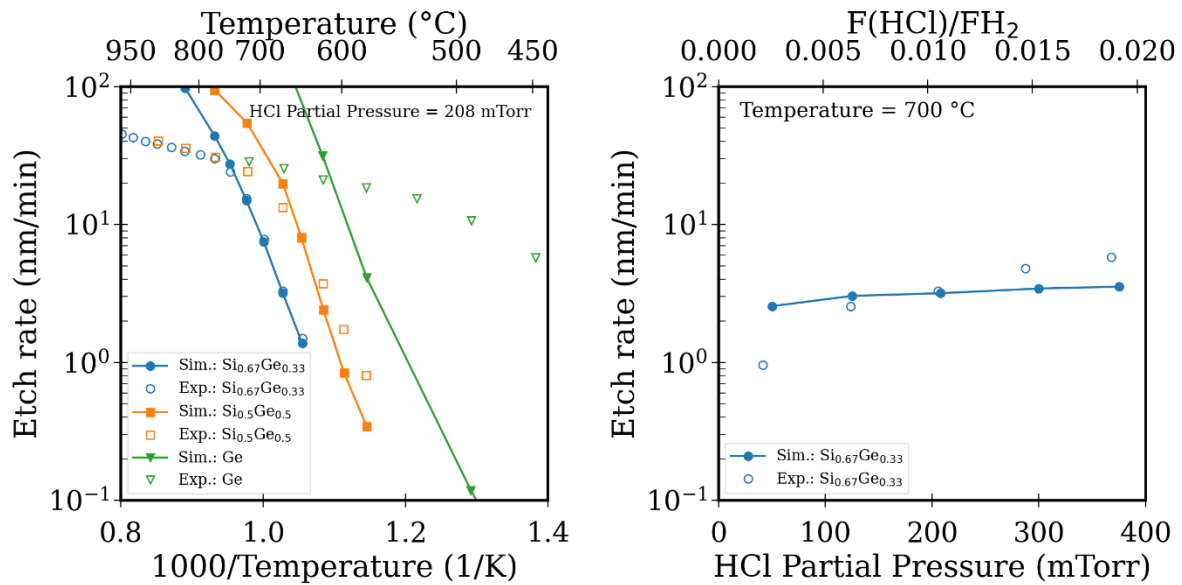*Figure 22: Simulated etch rate as a function of temperatures for $Si_{0.67}Ge_{0.33}$, $Si_{0.5}Ge_{0.5}$ and Ge (HCl partial pressure of 0.208 Torr, total pressure of 20 Torr) and etch rate as a function of HCl partial pressure for $Si_{0.67}Ge_{0.33}$ (temperature of 700 °C) using parameters set `calib_HCl_v2` reported in Table 4 (solid lines and full symbols). Experimental data, from [12], are plotted with empty symbols.*

Figure 22 shows the simulated etch rate $Si_{0.67}Ge_{0.33}$, $Si_{0.5}Ge_{0.5}$ and Ge as a function of temperature and HCl partial pressure, compared with experimental data [3]. The `calib_HCl_v3` set provides a good agreement for higher HCl partial pressures and temperatures up to 775 °C for $Si_{0.67}Ge_{0.33}$ and up to 675 °C for $Si_{0.5}Ge_{0.5}$. The low-temperature regime of HCl etching, i.e. the one characterized by a drastic dependence of the etch rate on the etch temperature [12], is well estimated for $Si_{0.67}Ge_{0.33}$, $Si_{0.5}Ge_{0.5}$, whereas the high-temperature regime, i.e. the one characterized by a small increase of the etch rate as the temperature increases [12], which is out of the scope of the present work, still needs further calibration efforts.

3.5 Simulation of the recipes

In this section, internal recipes for undoped and doped epitaxy of SiGe are simulated, first using AdvancedCalibration KMC and then the calibrations from the previous sections. We have 3 different recipes for undoped SiGe epitaxy (R1, R2, R3) and three for in-situ doped SiGe epitaxy (R4, R5, R6). We enable `LKMC_SiGe_Epitaxy` for the AdvancedCalibration calculations, and also use it as the basis for the calibrated simulations. All recipes use (001) Si as substrate.

3.5.1   Undoped SiGe epitaxy

For the undoped SiGe epitaxy, the recipes (R1, R2, R3) use H_2 as a carrier gas and DCS and germane as precursors. They aim for three different mole fractions (see Table 5) and differ in temperature and germane flow rate. For these recipes we focus on the growth rate and the germanium content as figures of merit. The results for all three recipes are shown in Table 5, at the top, we show the goal values for growth rate and Ge content, together with the measured values from X-ray reflectometry (XRR), X-Ray diffraction analysis (XRD), and Spectroscopic Ellipsometry (SE) measurements performed by LETI, which were already presented in D3.3. In the middle, the results from simulations with AdvancedCalibration KMC are shown and at the bottom, the simulation results with the additional calibration from Table 1 are shown.

Table 5: Growth rate and Ge content for the three undoped recipes (R1, R2, R3). The top part shows the goal values compared with the experimental results (XRR/XRD/SE) for the recipes, the middle part shows simulated results obtained by using AdvancedCalibration KMC, and the bottom part shows simulated results obtained with the additional calibration from Table 1.

	R1	R2	R3
Target / Experiment			
Growth rate (nm/min)	27.3 / 27.9	11.8 / 12.1	20.7 / 20.9
Ge content (%)	20 / 20.6	40 / 40.6	30 / 30.4
LKMC AdvancedCalibration KMC			
Growth rate (nm/min)	28.2	6.2	14.3
Ge content (%)	28.4	42.4	35.2
LKMC Additional Calibration			
Growth rate (nm/min)	35.3	7.0	16.9
Ge content (%)	25.6	40.5	32.8

The experimental results are very close to the respective goals. However, AdvancedCalibration KMC shows some serious deviations from experimental values: For R1 the growth rate is well reproduced, but the Ge content is 8% too high, a relative deviation of 40%. For both R2 and R3, the growth rates are significantly too low, while the Ge content is again too high. With the additional calibration for LKMC from Table 1 both the fits for the growth rate and Ge content of R2 and R3 are improved, while for R1, the growth rate is worse than for AdvancedCalibration KMC, but the Ge content is improved. We note that in experiment before epitaxy a surface preparation step is conducted. This is not described in simulation instead simulations start with a perfect surface, which is of course not the case in the experiments. As a result, growth rates in experiment are averaged values that can differ from the results obtained by simulations.

In general, it is impossible to have a calibration for all process conditions since several different simplifying assumptions went into the models. However, improving the quality of the calibration for a limited set of process conditions already allows to get an idea of the final structure after epitaxy and its properties, which is the main goal of these simulations.

3.5.2 *In situ* doped SiGe epitaxy

For the in-situ doped recipes (R4, R5, R6), again, H_2 is used as a carrier gas. The precursors are DCS, germane, HCl, and diborane. The recipes aim for three different B concentrations but the same germane content and differ in diborane flow rate. The growth rate, Ge content, and B concentration as well as the structural integrity of the epi layer are used as figures of merit. That the latter is a necessity can be seen in Figure 23, where the atomistic configuration of the epitaxial layer is shown. On the top, the full epitaxial layer is shown, while on the bottom, the layer is shown with Ge and Si atoms hidden. As can be seen in the bottom image, there is a structural problem, where below the surface, there is a thick layer of passivating species (black) including holes with a lot of passivating species well below the surface.
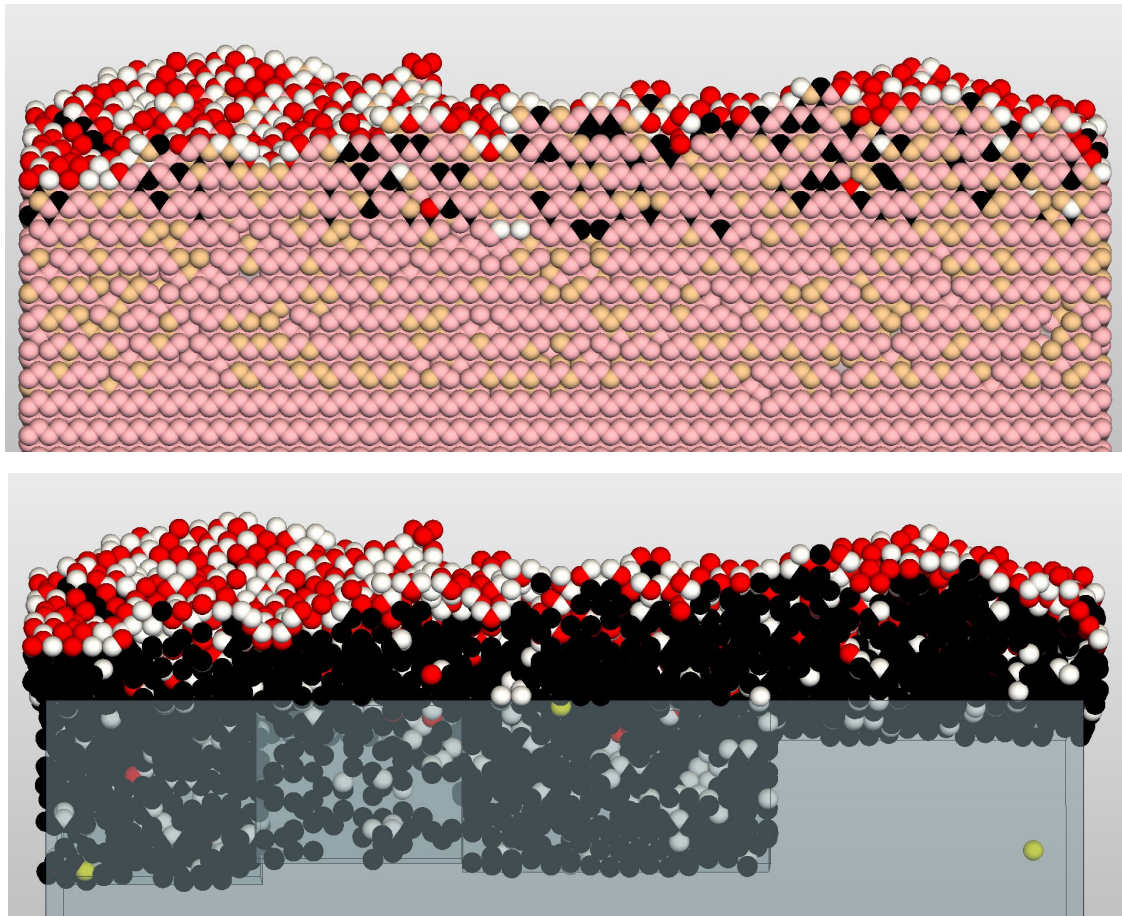
Figure 23: Picture of the atomistic configuration of the epitaxial layer resulting from R4. Black dots denote passivating species, red denotes hydrogen, white are surface sites. The other colors are Si, Ge, and B. (top) The full epi layer is shown, (bottom) the Ge and Si atoms were hidden, to get a better view into the layer.

In Table 6, we show the target values and the experimental results for the different figures of merit for the three recipes. In addition to XRR/XRD/SE measurements, we use results from Secondary Ion Mass Spectrometry (SIMS) measurements for experimental values of B concentration, which were also shown in D3.3. Note that we use the average B concentration over the thickness of the SiGe layer. For all three recipes the target values of growth rate and Ge content are well reproduced within the experiment. The B concentration, however, is significantly higher in experiment than the target values.

Table 6: Comparison of growth rate, Ge content, and B concentration for the in-situ doped recipes between experimental data from XRR/XRD/SE measurements, the target values for the recipes.

	R4	R5	R6
Target / Experiment			
Growth rate (nm/min)	5.23 / 5.26	5.8 / 5.75	6.4 / 6.38
Ge content (%)	30 / 32.7	30 / 31.6	30 / 29.8
B concentration (cm^{-3})	5e18 / 7.9e19	7e19 / 1.6e20	2.3e20 / 2.9e20
Structural integrity	Yes / Yes	Yes / Yes	Yes / Yes

These results are now compared to different calibrations, first the AdvancedCalibration KMC (see Table 7), then with the calibration for germane from Table 1 and with the default values for HCl (see Table 8). We then discuss simulations with the calibration for germane together with two different calibrations for HCl, the standard Si values (`calib_HCl_v1`), and the additional calibration from Table 3 (`calib_HCl_v2`)

Table 7: Simulation results with Advanced Calibration KMC for the growth rate, Ge content, and B concentration for the three in-situ doped recipes.

	R4	R5	R6
LKMC AdvancedCalibration KMC			
Growth rate (nm/min)	2.4	2.5	2.9
Ge content (%)	16.1	25.4	25.3
B concentration (cm^{-3})	5e18	5e19	1.2e20
Structural integrity	No	No	No

We find that AdvancedCalibration KMC strongly underestimates the growth rate, and – especially for R4 – the Ge content. For R4, the target B concentration is well reproduced, but for R5 and R6 it is slightly underestimated. The experimental B concentration, however, is strongly underestimated. For all three recipes, we obtain a very rough surface with a thick layer of passivating species and a few holes. The structural integrity of the layer is therefore not reproduced – as was shown in Figure 11.

Table 8: Simulation results with Advanced Calibration KMC and additional calibration for germane from Table 1 for the growth rate, Ge content, and B concentration for the three in-situ doped recipes.

	R4	R5	R6
LKMC Germane calibration			
Growth rate (nm/min)	2.7	2.5	2.8
Ge content (%)	15.3	15.3	18.2
B concentration (cm^{-3})	6.7e18	6.4e19	2.0e20
Structural integrity	No	No	No

Using only the calibration for germane (Table 1), we find a similar growth rate as with AdvancedCalibration KMC. The Ge content is even lower, only about half of the target value. A slightly lower Ge content could have been expected, based on the fact that due to the calibration of germane parameters the Ge content slightly fell, however, such a stark decrease in the Ge content is still surprising. The B concentration is increased, so that it is generally a rather good fit to the target values, but still highly underestimated for the experimental values.

When using the calibrated germane parameters together with the parameters for HCl from `calib_HCl_v1` or `calib_HCl_v2` a new problem arises: The growth has a maximum, after which the epi layer slowly declines, and no further growth is happening. This maximum is usually reached after a minute of growth and is usually at a layer thickness of about 1.5 nm. The Ge content in this thin layer is below 1 %, and the B concentration is non-existent. It should be noted that this result is in clear contradiction to the results from Section 3.4 because there it was shown that for `calib_HCl_v1` the etch rate is way below the one from the default parameters from AdvancedCalibration KMC. It is unclear where this discrepancy is coming from.

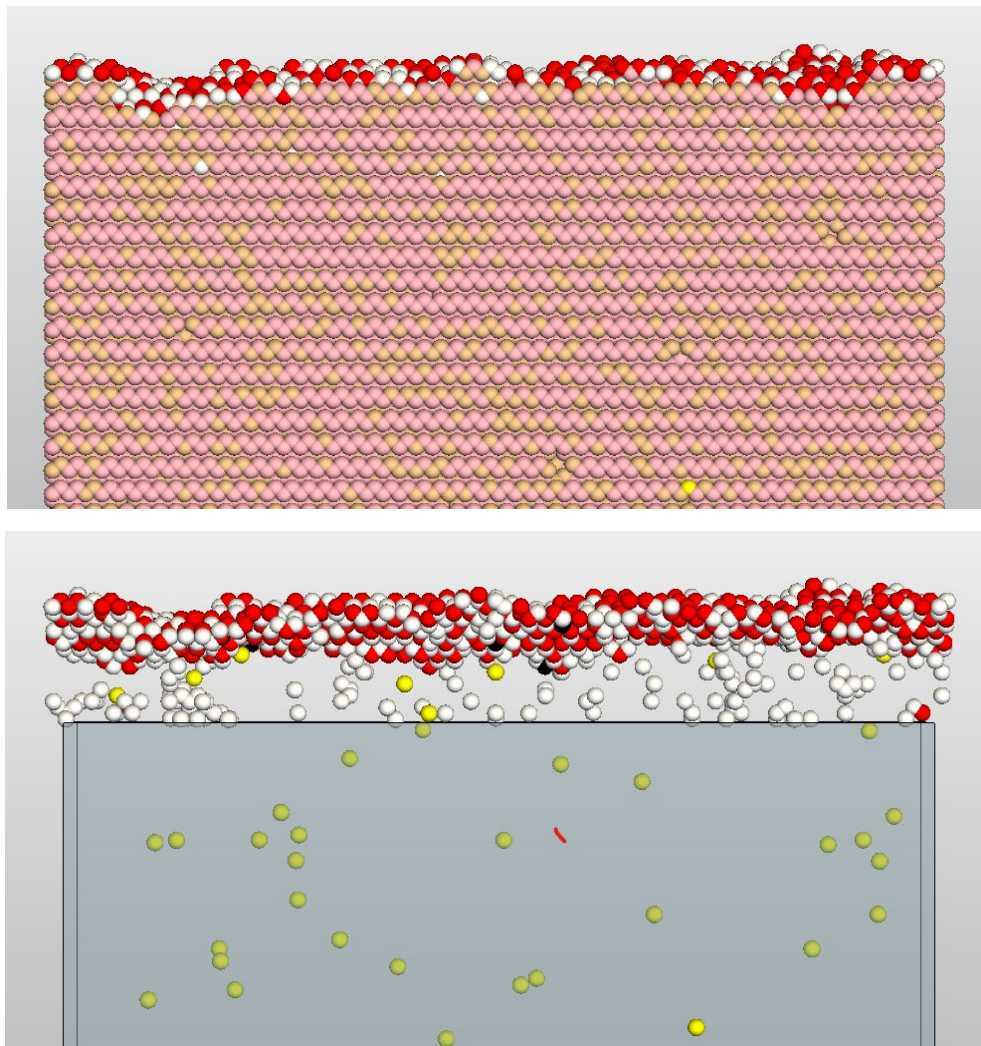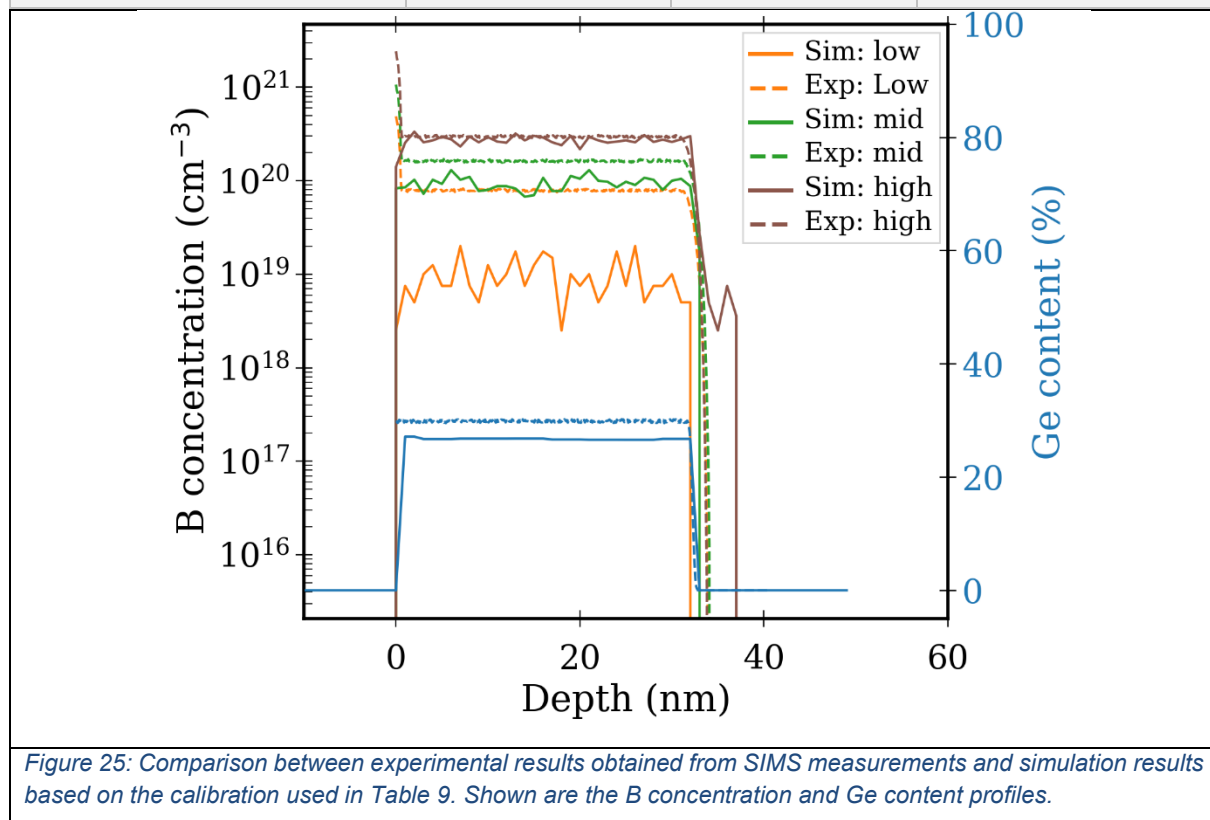*Figure 24: Picture of the atomistic configuration of the epitaxial layer resulting from R4 with the calibration of germane parameters and without HCl in the recipe. Black dots denote passivating species, red denotes hydrogen, white are surface sites. The other colors are Si, Ge, and B. (top) The full epi layer is shown, (bottom) the Ge and Si atoms were hidden, to get a better view into the layer.*

Table 9: Simulation results with Advanced Calibration KMC and additional calibration for germane from Table 1 and without HCl as a precursor for the growth rate, Ge content, and B concentration for the three in-situ doped recipes.

	R4	R5	R6
LKMC Germane calibration + no HCl			
Growth rate (nm/min)	11.1	11.1	11.2
Ge content (%)	26.7	26.9	26.9
B concentration (cm^{-3})	9.7e18	9.2e19	2.4e20
Structural integrity	Yes	Yes	Yes

Figure 25: Comparison between experimental results obtained from SIMS measurements and simulation results based on the calibration used in Table 9. Shown are the B concentration and Ge content profiles.

Since all these parameter sets have significant problems, and since discussions with Synopsys showed, that there is some form of problem with HCl implementation – the extent of which we are not familiar with – we suggest for the time being to not include HCl in the simulation, even when HCl is included in the original recipe. For the three in-situ doped recipes we find – without HCl but including the calibration of germane parameters – the results are shown in Table 9 and Figure 25.

The growth rate is a too large by a factor of two. As a result, we adapted the growth time in simulations to receive the correct layer thickness based on this increased growth rate. The Ge content is rather well reproduced, with only a few percent below the experimental values. Since the profiles for the Ge content coincide for the three recipes, we only show the case of R4 in the graph. The B concentration is higher than the target values, which is in line with the experimental results. For R4 it is still significantly too low to match the experimental values, but the results are the best of any calibration shown this far. We note that it is surprising that

the experimental value is so much above the target value. For R5 and R6 the B concentration is well reproduced in simulation assuming an error in SIMS measurements of the B concentration of about 10-20 % of the nominal concentration – this is especially true in the case of the high doping levels from R6. Finally, the structural integrity is kept, the surfaces are smooth and there is no thick layer of passivating species below the surface, as can be seen in Figure 24.

Just as in the case of the growth of undoped epitaxial layers, we note that this improvement allows us to get a prediction of the resulting structure and its properties. However, here the main issue is that due to limitations in the Sentaurus TCAD software, the impact of HCl cannot be properly modeled. This is a major drawback, especially with respect to the simulation of the demonstrators in WP6. Nonetheless, the approach taken here should be sufficient for these simulations – especially for intermediate to high doping levels – and further approaches are also possible, e.g., using a less sophisticated model in Sentaurus Process or employing `MulSKIPS` as an alternative.

4. Calibration and simulations of epitaxial growth using `MulSKIPS`

This section will be dedicated to the formulation of super-Lattice Kinetic Monte Carlo (KMCsL) models for the simulation of Chemical Vapor Deposition (CVD) epitaxy in Si and SiGe structures using the open-source package `MulSKIPS` [14], developed by the CNR. The main advantage of KMCsL approaches, which makes them suitable for multi-scale processes like CVD, is the possibility to simulate time and space scales much wider than *ab initio* methods, with atomistic details, including defective configurations, not accessible to continuum and standard LKMC approaches. These features could allow the achievement of a complete process simulation, bridging machine and feature scales, with structural properties predicted with atomic accuracy. A delicate point concerns the multi-step nature of epitaxial processes, characterized by multiple chemical reactions occurring in the vapor phase and at the solid-vapor phase boundary, which must be considered for reliable simulations. Indeed, such reactions have a strong impact on the growth (etch) kinetics as well as on the final morphology of the grown material. This consideration holds even for a fixed precursor chemistry, as the final products will vary both on the initial composition (in terms of partial pressures) and on the temperature.

Here we propose a method to simulate with atomic resolution the kinetics of CVD growth or etch processes for group IV compound semiconductors and in general materials with tetrahedral bonding, such as (pristine or doped) Si, Ge, or $Si_{1-x}Ge_x$, but also SiC, GaAs, GaN, and others. Such methodology has been entirely developed during the MUNDFAB project and relies on an extension of the `MulSKIPS` code, already demonstrated for Physical Vapor Deposition (PVD) and Laser Annealing (LA) processes [15, 16, 17]. Distinctive features of epitaxial processes, namely the presence of coverage species adsorbed to the evolving surface, as well as chemical reactivity in the bulk gas phase and at the gas-solid interface, are reproduced through a proper definition of the Monte Carlo (MC) particles and of the corresponding event probabilities, calibrated against experiments. We apply the method to the $H_2+HCl+SiH_2Cl_2$ chamber chemistry as an example.

The source code and all Jupyter notebooks needed to reproduce the calibration workflow and the simulations presented in this report can be accessed through the online public Github repository of `MulSKIPS` [14].

4.1   The KMCsL model of CVD epitaxy in `MulSKIPS`

A distinctive feature of the `MulSKIPS` code is the adoption of a super-lattice formalism, able to model the regular lattice of the ideal crystal as a sub-lattice of a cubic superlattice [17]. This allows to locally reconstruct point-like and extended defective configurations, as they emerge from the reconfiguration of atom positions and bonding in the super-lattice, without labeling the substrate lattice points, under the assumption of a symmetric tetrahedral bonding configuration. Indeed, as described below, defect formation can be introduced by allowing for a small probability of armchair-type bonding between adjacent ad-atoms (while the more energetically favorable zigzag configuration leads to the ideal defect-free crystal structure). The model assumption is that growth (etch) occurs at the interface between the crystal and gas phases because of a balance between atom-by-atom transitions from one phase to the other. The system evolution is driven by three types of active MC particles, defined on the solid-gas interface, which are schematically illustrated in Figure 26, along with the associated MC events:

a) "crystal ad-atoms": occupied undercoordinated (i.e., with 1 to 3 nearest neighbors) semiconductor atoms (like Si, Ge, or B);

b) "coverage ad-atoms": occupied undercoordinated non-crystalline species (such as H or Cl) derived from the precursor molecules;

c) "ad-voids": empty super-lattice sites which connect to an ad-atom by one of its dangling bonds.
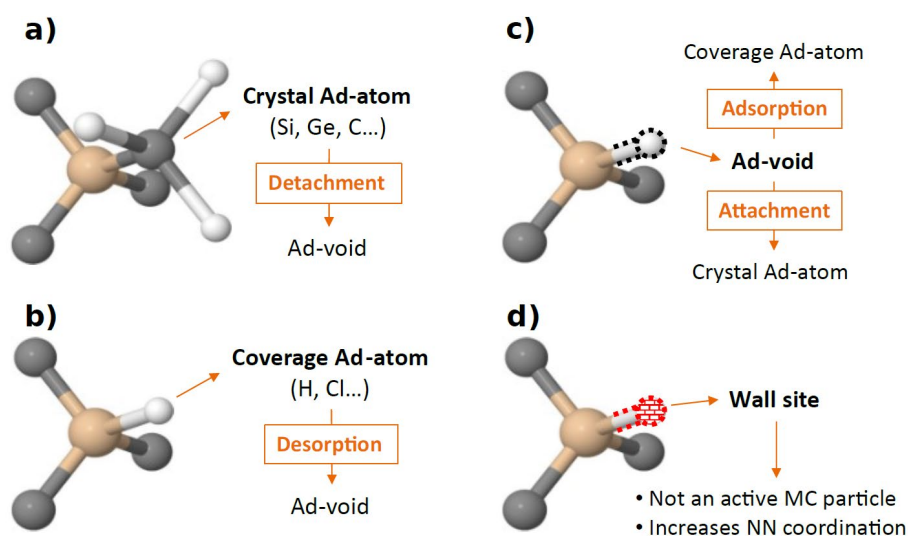
Figure 26: Particle types implemented in the `MulSKIPS` KMCsL framework. The kinetic events eligible for each particle are indicated, along with the resulting particle states. (a) Crystal ad-atoms are active MC particles that can only undergo detachment events, turning into ad-voids. (b) Coverage adatoms can only undergo desorption events, turning into ad-voids. (c) Ad-voids can undergo either attachment events, turning into crystal ad-atoms, or adsorption events, turning into coverage ad-atoms. (d) Wall sites are not active MC particles. Their position is fixed for the whole duration of the simulation and their role is to increase by one the coordination of all nearest crystal or coverage ad-atoms.

An active MC particle can undergo four possible events during a CVD growth (etch) simulation (see Figure 26):

i) "attachment" of a crystal-type atom from the gas phase to an ad-void;

ii) "detachment" of a crystal ad-atom, which turns from the solid to the gaseous phase;

iii) "adsorption" of a coverage-type atom to an ad-void;

iv) "desorption" of a coverage ad-atom, which returns to the gas phase.

In addition to the active MC particles, the `MulSKIPS` code allows the introduction of "wall sites" (Figure 26), to define non-evolving regions in the simulation box. Their position is fixed for the whole duration of the simulation and their action is to simply increase by one the coordination number (Coor) of all the nearest active MC particles. All types of active MC particles are treated at the same level and stored in the same "ListAdAtom" list, whereas four-fold coordinated "bulk" crystal ad-atoms are stored in a separate "ListAtom" and four-fold coordinated ad-voids (i.e., vacancies) are stored in a "ListVoid" list. Particles in the latter two lists can be promoted to active MC particles and enter the "ListAdAtom" list whenever one of their four nearest-neighbor (NN) crystal ad-atoms undergoes a detachment event. All these lists contain the particle (x,y,z) lattice coordinates, those of their NN sites and, in the case of "ListAdAtom", also the event type scheduled for the MC particle and the corresponding probability. The occupancy state, the coordination value as well as the type of each particle (namely crystal, coverage or wall) is bit-encoded in an integer, which is in turn stored in a 3D array "LattCoo" and indexed by the particle (x,y,z) coordinates. By accessing the information stored in the aforementioned lists, it is possible to update the state of the KMCsL particles and their NN atoms on-the-fly after every stochastic event selection.

The introduction of ad-coverage species and adsorption/desorption events represents the main difference with respect to the KMCsL implementation for PVD processes [15]. Notice that all the actions undertaken in the code during attachment and detachment events are not affected by the introduction of coverage ad-atoms in the simulations. However, important modifications are made to non-coverage MC particles when an adsorption or desorption event is selected. In particular, an adsorption event, besides converting an ad-void into a coverage ad-atom, has the effect of modifying the detachment probability of its NN crystal ad-atoms, according to user-defined instructions given at the calibration stage (see below). Importantly, the adsorption of coverage ad-atoms does not alter the coordination value of the NN crystal ad-atoms. In this way, even if the coverage ad-atom occupies the last available empty dangling bond of a crystal ad-atom with Coor=3, the latter will still remain an active MC particle able to detach from the surface. Moreover, coverage ad-atoms are prevented from having NN ad-voids or coverage ad-atoms. Consequently, the surface growth (etch) rate, governed by the attachment/detachment ratio of crystal ad-atoms at the solid-gas interface, is hindered by the presence of coverage ad-atoms occupying otherwise available empty sites at the solid-gas interface, in line with experimental observations.

As for PVD simulations [17], the formation of stacking defects can be accounted for in `MulSKIPS`. Two tetrahedral bonding configurations are allowed in the KMC super-lattice, namely that of cubic (zinc-blend) or hexagonal (wurtzite) crystal phases. Whenever a deposition event occurs on a site S with Coor=1, its bonding configuration with potential neighbors is set to either cubic or hexagonal, depending on the surrounding environment. If the bonding configurations of its next neighbors are mostly set to cubic (hexagonal), then the stacking choice made for the S site will be cubic (hexagonal). Instead, if the bonding configurations of its next-neighbors are equally distributed between cubic and hexagonal, then there is a user-defined probability *Ptranszig* to initiate a new phase. Importantly, reciprocity is always imposed when choosing the bonding configuration: a bond can form only if two next neighbors point the relative orbitals in the same direction.

Notice that, since only atomic species are eligible as active MC particles, molecular species and their reactivity cannot be described explicitly. Molecular fluxes and chemical reactions

occurring in the gas phase and at the evolving crystal-gas interface are therefore translated into fluxes of individual atomic species reaching the surface and undergoing single-atom phase transitions. The transition events are selected stochastically according to predefined probability tables, which are carefully calibrated to account for all possible chemical phenomena occurring during the CVD process, within a given precursor environment and under given thermodynamic conditions. The calibration strategy is discussed below.

4.2 Calibration strategy and tools

A proper calibration strategy is crucial to couple the reactor-scale features of the process to the atomic scale of MC transition probabilities and material morphology.

We followed a stepwise approach (summed up in Figure 27):

1. Collection of an experimental database for planar Si growth (etch) from the chosen precursors at varying pressures and temperatures;

2. Calculation, for each experiment, of the bulk gas phase equilibrium composition;

3. Analytical model of Si growth (etch), based on the surface reactions of the equilibrium gas species;

4. Definition and calibration of the corresponding MC event probabilities.

5. KMCsL simulation of a specific CVD process and geometry
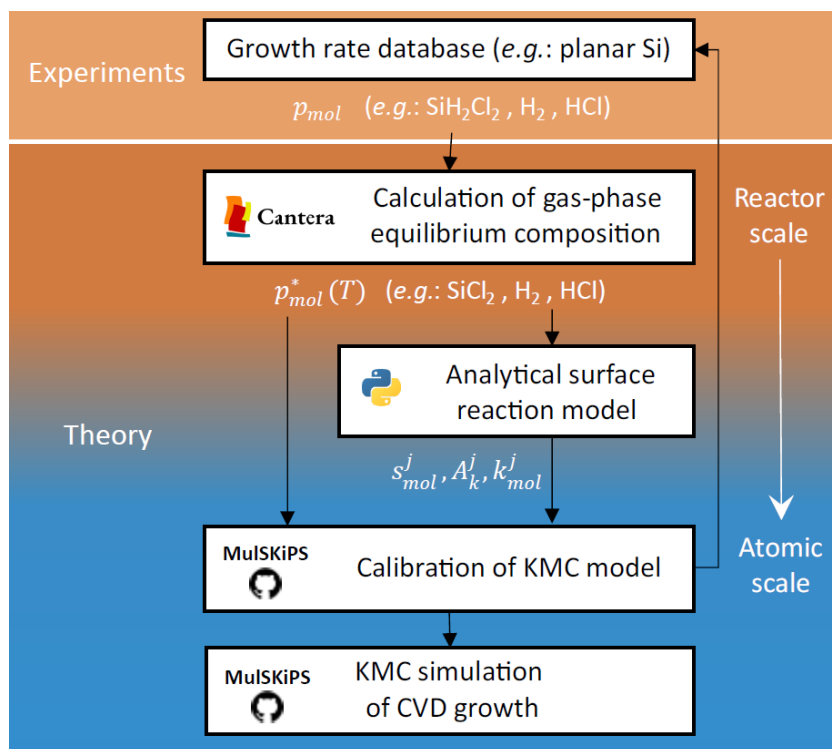
Figure 27: Schematics of the calibration procedure, detailed in the main text, enabling the translation of the reactor-scale features of the experiment (notably temperature and precursor pressures p_{mol}) into KMC event rates that can be used to predict the growth kinetics with atomistic detail.

The so-calibrated KMCSL model can be used to simulate different process conditions and/or substrate geometries involving the chosen precursor chemistry. In this study we consider the

case of H_2 + HCl + SiH_2Cl_2 as an example, but the approach can be generalized to different precursors with system-specific adjustments.

4.2.1   Calculation of gas-phase equilibria

The first calibration step consists of the steady-state calculation of chemical reactions in the gas phase. This allows, given the chosen experimental conditions (precursor species, pressure, and temperature), to identify the gas species that are more likely to interact with the evolving surface. At this stage, we neglect thermo-fluid dynamics transport in the reactor. This aspect, which is especially relevant for confined geometries, may be included in future development of the code by appropriately coupling to external mass transport tools.

To implement gas-phase homogeneous reactions in our code, we took advantage of the open-source software Cantera [18], imported in a dedicated Python routine following the provided documentation. All the species potentially involved in gas-phase equilibria for the chosen precursor chemistry and all the corresponding reactions were embedded in a customized database. For each species, the database reports the element composition and the 7-Coefficient NASA polynomial parameterization for various temperature ranges (from 300 to 5000K) [19], which are used to calculate its thermodynamic properties (molar heat capacity at constant pressure, molar enthalpy, and absolute molar entropy). For each reaction, the stoichiometry, reaction order and Arrhenius parameters (pre-factor and energy barrier) are reported, distinguishing between forward and backward reactions. These parameters are used by Cantera to calculate the rate constant k of each reaction (back and forward) and, consequently, the molar fractions χ_* of product species, as a function of the molar fractions χ of the reactants and of the process temperature T.
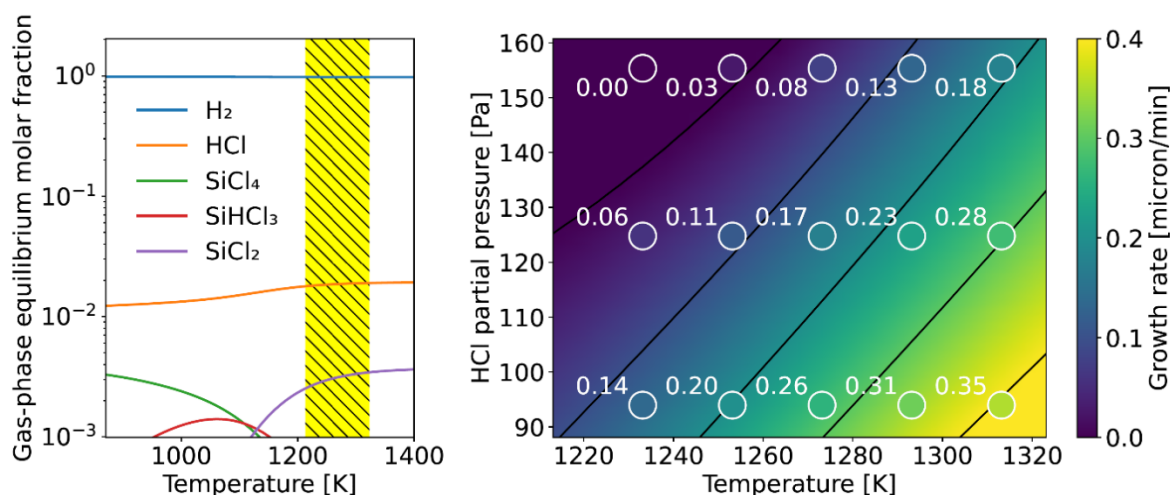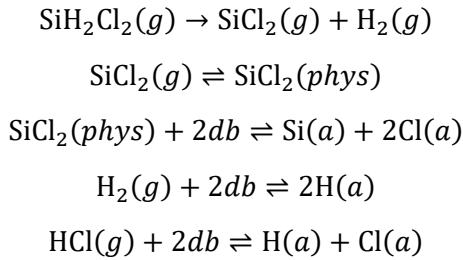

Figure 28: Example of gas-phase steady-state calculation results. Mole fractions of reaction products as a function of temperature (in K), obtained from an initial mixture of H_2 (7813Pa), HCl (155Pa), and SiH_2Cl_2 (31Pa). Calculations were run with Cantera [18] and involved 24 chemical species and 40 chemical reactions, among the hundreds listed in our database. Only the species above a molar fraction threshold of 10^{-3} are displayed. Notice that the final gas composition is temperature dependent. In the temperature range of all the experiments considered for calibration in this work (yellow area), the mixture components are H_2, HCl and $SiCl_2$. The right panel shows the growth rate calculated from the analytical model of surface reactions while fixing the above recipe but varying the HCl partial pressure. Contour lines correspond to the ticks' values in the color bar. The circles represent growth rates measured at 155 Pa, 125 Pa and 94 Pa HCl partial pressure. The analytical model reasonably reproduces the expected trend of increasing growth rate with decreasing HCl pressure, as well as their expected temperature dependence.

An example of our calculation output for the H_2 + HCl + SiH_2Cl_2 chemistry is provided in Figure 28. For an initial mixture of H_2 (7813 Pa), HCl (155 Pa) and SiH_2Cl_2 (31 Pa) and temperatures above 1200 K, the main species in the mixture at equilibrium are always found to be H_2, HCl and $SiCl_2$. Hence, under these thermodynamic conditions, the latter three species should be considered as those actually reaching the surface and contributing to their local evolution.

4.2.2 Analytical model of surface reactions

Based on the results of gas-phase equilibrium calculations, we wrote a 0D analytical model of growth of a flat Si substrate, accounting for the attachment/detachment of the precursor species – here $SiCl_2$, HCl and H_2. The following simplified reaction sequence was used:

$$SiH_2Cl_2(g) \rightarrow SiCl_2(g) + H_2(g)$$

$$SiCl_2(g) \rightleftharpoons SiCl_2(phys)$$

$$SiCl_2(phys) + 2db \rightleftharpoons Si(a) + 2Cl(a)$$

$$H_2(g) + 2db \rightleftharpoons 2H(a)$$

$$HCl(g) + 2db \rightleftharpoons H(a) + Cl(a)$$

where g stands for bulk gas phase; $phys$=physisorbed state, a=adsorbate, db=dangling bond; double-headed arrows indicate reversible reactions, single-headed arrows denote irreversible reactions. Assuming a precursor-mediated adsorption/desorption mechanism for $SiCl_2$, HCl and H_2, the previous reactions lead to the following system of coupled differential equations in the surface coverages Θ_i, with i = H,Cl,Si, where SiH_2Cl_2 is assumed instead of $SiCl_2$:

$$\frac{d\Theta_H}{dt} = 2s_{H_2}F_{H_2}^* + s_{HCl}F_{HCl}^* - 2k_{H_2}\Theta_H^2 - k_{HCl}\Theta_{Cl}\Theta_H$$

$$\frac{d\Theta_{Cl}}{dt} = 2s_{SiCl_2}F_{SiCl_2}^* + s_{HCl}F_{HCl}^* - 2k_{SiCl_2}\Theta_{Cl}^2 - k_{HCl}\Theta_{Cl}\Theta_H$$

$$\frac{d\Theta_{Si}}{dt} = s_{SiCl_2}F_{SiCl_2}^* - k_{SiCl_2}\Theta_{Cl}^2 \qquad (1)$$

Here, $F_i^* = \frac{p_i^*}{\sqrt{2\pi M_i RT}}$ is the impingement flux of the precursor species i (stars referring to the gas-phase equilibrium values in the mixture, obtained from Cantera outputs, with partial pressures $p_i^* = p_{tot}\chi_i^*$); $k_i = A_i e^{-\varepsilon_i/k_B T}$ is a kinetic desorption constant; s_i is the so-called reactive sticking coefficient of i, whose simplest form is:

$$s_i = s_i^0 \Theta_{db}^{free}$$

with Θ_{db}^{free} being the surface density of available dangling bonds and s_i^0 the initial sticking coefficient, which can be written as:

$$s_i^0 = \frac{\alpha_i}{1 + \beta_i \exp[-\epsilon_i/RT]}$$

where α_i, β_i and ϵ_i are i-dependent parameters, assumed to remain constant over the whole temperature range.

Concerning surface coverage, the saturation values (and hence Θ_{db}^{free}) depend in principle on both the species i (e.g., H vs Cl) and the precursor for a given species (e.g., HCl vs Cl_2 or SiH_2Cl_2). As a first approximation we assume that both H and Cl saturate the surface upon formation of a monolayer, regardless of the precursor, and that the total coverage saturates at

$$\Theta_{\text{sat}} = \Theta_{\text{db}}^{\text{tot}} = \Theta_{\text{Cl}} + \Theta_{\text{H}} + \Theta_{\text{db}}^{\text{free}}$$

with Θ_{db}^{tot} coinciding with the surface density of dangling bonds for the chosen orientation of the crystal substrate, namely $\Theta_{db}^{tot} = 6.78 \times 10^{18}$ m^{-2} for (100) [20] and $\Theta_{db}^{tot} = 1.1 \times 10^{18}$ m^{-2} for (111) [21].

A steady-state equilibrium condition is assumed. Posing $\frac{d\Theta_{\text{H}}}{dt} = 0$ and $\frac{d\Theta_{\text{Cl}}}{dt} = 0$, coverage concentrations for hydrogen and chlorine satisfy the following set of algebraic equations:

$$2k_{\text{SiCl}_2}\Theta_{\text{Cl}}^2 + k_{\text{HCl}}\Theta_{\text{H}}\Theta_{\text{Cl}} = \left(2s_{\text{SiCl}_2}F_{\text{SiCl}_2}^* + s_{\text{HCl}}F_{\text{HCl}}^*\right)$$

$$2k_{\text{H}_2}\Theta_{\text{H}}^2 + k_{\text{HCl}}\Theta_{\text{H}}\Theta_{\text{Cl}} = \left(2s_{\text{H}_2}F_{\text{H}_2}^* + s_{\text{HCl}}F_{\text{HCl}}^*\right)$$

According to this model, $\frac{d\Theta_{\text{Si}}}{dt}$ is proportional to the Si growth rate, by a factor equal to the inverse of the density of the material, $\rho_{\text{Si}}^{\text{at}} = 5.02 \times 10^{28}$ m^{-3}. Hence, the growth rate can be calculated by solving the system of the previous two algebraic equations, substituting Θ_{H} and Θ_{Cl} into the differential equations for the surface coverage and dividing by $\rho_{\text{Si}}^{\text{at}}$.

The right panel in Figure 28 shows the growth rate calculated from the analytical model of surface reactions while fixing a partial pressure of 7813 Pa for H$_2$ and 31 Pa for SiH$_2$Cl$_2$, respectively, and varying the HCl partial pressure. Growth rates measured at 155 Pa, 125 Pa and 94 Pa HCl partial pressure are also reported for comparison. The analytical model reasonably reproduces the expected trend of increasing growth rate with decreasing HCl pressure, as well as their expected temperature dependence. Slight deviations (below 0.5 µm/min) are only found for low HCl pressure at the highest considered temperatures.

Importantly, when simulating different process conditions where different gas species (other than SiCl$_2$, HCl and H$_2$) are present in the equilibrium gas mixture, the current model must be corrected to account for those species (and the corresponding model parameters must be calibrated accordingly).

4.2.3   Definition and calibration of MC event rates

The outputs of gas-phase calculations and the surface reactions analytical model provided a starting point for the KMCsL model calibration. The frequencies of the MC events described previously were defined as follows:

    i)   Attachment probability

$$v_{\text{att}}^i(n) = B_0 \sum_{\text{mol}} c_{\text{mol}}^i \frac{p_{\text{mol}}^*}{\sqrt{2\pi M_{\text{mol}}RT}} s_{\text{mol}}^i$$

    ii)   Detachment probability:

$$v_{\text{det}}^i(n) = B_0 \cdot B_1 \Theta_{\text{sat}}^2 \cdot e^{-E_{\text{det}}(n)/k_BT} \sum_{\text{mol}} c_{\text{mol}}^i A_{\text{mol}} e^{-\varepsilon_{\text{mol}}/k_BT}$$

    iii)   Adsorption probability:

$$v_{\text{ads}}^j(n) = B_0 \sum_{\text{mol}} c_{\text{mol}}^j \frac{p_{\text{mol}}^*}{\sqrt{2\pi M_{\text{mol}}RT}} s_{\text{mol}}^j$$

    iv)   Desorption probability:

$$v_{\text{des}}^{j}(n) = B_0 \cdot B_1 \Theta_{\text{sat}}^2 \sum_{\text{mol}} c_{\text{mol}}^{j} A_{\text{mol}} e^{-\varepsilon_{\text{mol}}/k_B T}$$

where n is the coordination number of the crystal ad-atom involved in the transition; mol are the major gas-phase species at equilibrium, with molar mass M_{mol} and partial pressure p_{mol}^*; $c_{\text{mol}}^{i(j)}$ is the stoichiometric coefficient of species i (j) in molecule mol, superscripts i and j denoting crystal and coverage species, respectively; s_{mol}^{i} is the sticking coefficient, as appearing in the differential equations of the surface coverage; A_{mol} and ε_{mol} are the prefactors and energy barriers of the desorption coefficients k_{mol} appearing in the differential equations of the surface coverage; the term $B_1 \Theta_{\text{sat}}^2$, with B_1 being a constant, is a conversion factor that ensures that the desorption rate in the KMCsL formulation has the same units as the desorption rate in the equations used in the analytical model (negative terms in Eq. (1)); B_0 is a scaling factor, equal for all the MC processes; k_B and R are the Boltzmann and gas constants and T the process temperature; $E_{\text{det}}(n)$ is a coordination-dependent detachment barrier.

Most of the above parameters are found after step 3 of the workflow, by calibrating the analytical model on the measured temperature-dependent growth rate. The only parameters specific to the KMCsL model, to be calibrated at step 4 of the workflow, are B_0, B_1 and $E_{\text{det}}(n)$. The latter corresponds to a matrix of coordination-dependent detachment probabilities which, in the simplest case, do not distinguish between different neighbor species, reducing to 3 values only, $E_{\text{det}}(1)$, $E_{\text{det}}(2)$ and $E_{\text{det}}(3)$. In this work, to keep the number of calibration parameters as low as possible, we introduce only one exception to this simplified framework in the cases where the local neighbor configuration would favor the desorption of the crystal species in a stable molecular form. Since Si atoms in our model can only detach from the surface in the form of $SiCl_2$ molecule (see negative term on the right side of Eq. (1), we indeed set $E_{\text{det}} \equiv E_{\text{det}}(2) - \Delta E$ for all Si atoms ending up with 2 Cl neighbors during the simulation, with ΔE being an additional calibration parameter.

We remark that the full matrix of KMCsL probabilities (not only the detachment ones) can in principle be defined to depend on the neighbor chemical environment (e.g., chemical type and bonding coordination). This significantly increases the number of potential knobs to turn and makes the CVD framework readily applicable to other crystal-precursors combinations.

4.3　Results and discussion

The results of step 3 and step 4 of the calibration workflow are reported in Figure 29, for a CVD process of Si (001) at a total pressure of 7999 Pa and H_2 (p=7813Pa), HCl (p=155Pa) and SiH_2Cl_2 (p=31Pa) initial precursors (the same mixture as in Figure 28), considering a temperature range where the dominant gas species are represented by H_2, HCl and $SiCl_2$.

The set of parameters used in the analytical model (step 3 of the workflow) are:

$A_{H_2} = 2.4 \times 10^{-4} \text{m}^2\text{s}^{-1}$,　　　$A_{SiCl_2} = 8.4 \times 10^{-6} \text{m}^2\text{s}^{-1}$,　　　$A_{HCl} = 6.6 \times 10^{-3} \text{m}^2\text{s}^{-1}$,

$\varepsilon_{H_2} = 2.69 \text{ eV}$,　　　　　　　$\varepsilon_{SiCl_2} = 2.91 \text{ eV}$,　　　　　　$\varepsilon_{HCl} = 3.12 \text{ eV}$,

$\alpha_{H_2} = 9.7 \times 10^{21}$,　　　　　$\alpha_{SiCl_2} = 2.6 \times 10^{23}$,　　　　$\alpha_{HCl} = 2.7 \times 10^{22}$,

$\beta_{H_2} = 1.2 \times 10^{9}$,　　　　　　$\beta_{SiCl_2} = 6 \times 10^{2}$,　　　　　$\beta_{HCl} = 8.4 \times 10^{6}$,

$\epsilon_{H_2} = 1.57 \text{ eV}$,　　　　　　$\epsilon_{SiCl_2} = 0.165 \text{ eV}$,　　　　$\epsilon_{HCl} = 1.6 \text{ eV}$.

The additional 6 KMCsL-specific parameters are:

$$B_0 = 1.6 \times 10^{-19}, \qquad B_1 = 0.1, \qquad \Delta E = 0.5 \text{ eV},$$

$$E_{\text{det}}(1) = -0.4 \text{ } eV, \qquad E_{\text{det}}(2) = 0.3 \text{ eV}, \qquad E_{\text{det}}(3) = 1.11 \text{ eV}.$$

The coverages Θ_H and Θ_{Cl} as a function of temperature are shown in Figure 29 (left), along with the overall surface coverage ($\Theta_H + \Theta_{Cl}$). These curves reflect a clear tendency to desorb H and Cl species as temperature increases, and higher Cl coverage compared to H. Remarkably, these results demonstrate that, despite the significant intrinsic differences between analytical and KMCsL approaches, the two models provide quite similar results if calibrated using the proposed workflow. A reasonably good agreement between the two models can also be observed when comparing the growth rates obtained as a function of temperature. This is shown in Figure 29 (right), where the experimental data used as a reference for the calibration are also reported (growth rates indirectly measured via spreading resistance profiling at STMicroelectronics in Catania). Figure 29 (right) also demonstrates a strong correlation between the trends of growth rate and surface coverages as a function of temperature. The growth is indeed slower at lower temperatures, where a larger saturation of surface dangling bonds by coverage species occurs and where a higher ratio between Cl and H coverages favors detachment events in the form of $SiCl_2$. Both the analytical and the KMCsL model predict a negative growth rate in the temperature range where no growth was measurable (below ~1260 K). This can be attributed to Cl-mediated surface etching, which is modeled in our simulations but could not be carefully assessed in the experiment due to the negligible variation in measured layer thickness. Compared to the analytical model, the KMCsL predicts a quite lower etching velocity.

All the advanced KMCsL CVD simulations presented in the following sections are obtained by considering a temperature of 1263 K, where the gas-phase equilibrium calculation yields H_2, HCl and $SiCl_2$ as dominant molecular species, with p_{H2} = 7820 Pa, p_{HCl} = 148 Pa, p_{SiCl2} = 25 Pa.
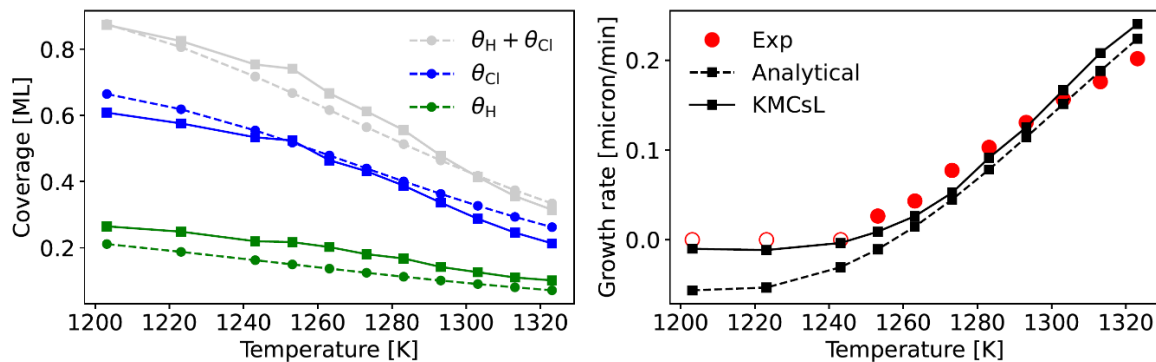

Figure 29: Results of the workflow for a CVD growth of Si (001) from H_2 (p=7813Pa), HCl (p=155Pa) and SiH_2Cl_2 (p=31Pa). Left: H (green) and Cl (blue) coverages and total (grey) surface coverage ($\theta_H + \theta_{Cl}$) predicted by the analytical model (dashed lines) and the KMCsL model (solid lines). Right: growth rate as a function of temperature predicted by the KMCsL model (black solid line), compared to the experimental data (red circles) and the predictions of the analytical model (black dashed line). Empty red circles indicate temperatures at which no growth could be measured.

4.3.1 KMCsL CVD simulations of Si (001) with stacking defects

In this section we show that the atomistic framework presented so far can be applied to simulate defective CVD growth. We consider a model of a Si(001) surface, represented via a KMCsL cell of 21 x 21 x 43 nm^3, periodic along x and y (see Figure 30). In order to maximize the probability of forming stacking defects, we structure the initial surface as a 2D array of inverted pyramids with faces along the ⟨111⟩ directions. The latter only exposes sites with Coor=1, which are those allowed to trigger polymorphic transitions from cubic to hexagonal crystal phases and *vice versa* (see Section 4.1). Figure 30 shows the initial and final state of the solid-gas interface in a simulation of ~26 s with a `Ptranszig`=0.95. A self-closing triple stacking fault is generated during the growth, with the typical hexagonally stacked crystal layer highlighted in purple. Vacancies are also formed during the process simulation, shown in red, representing empty sites that get surrounded by filled sites with Coor<4 during the simulation. We note that their density in an actual CVD process might be lower, due to their possible diffusion towards the surface (not implemented in the current model).
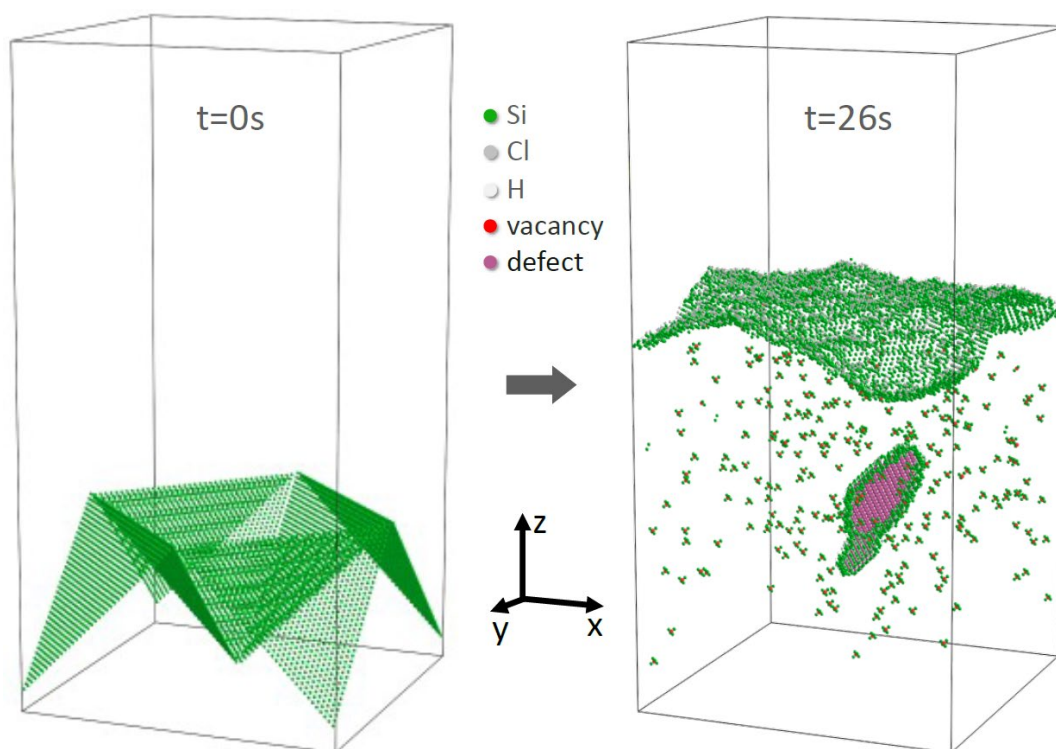

Figure 30: KMCsL simulation of CVD growth from a Si inverted pyramid substrate, obtained imposing p_{H2}=7813Pa, p_{HCl}=155Pa, $p_{SiH2Cl2}$=31Pa, T=1263K and allowing for defect formation (`Ptranszig`=0.95). Left: input substrate geometry (.xyz file), made of (111)-oriented Si surfaces. Right: system evolution after a 26s simulated growth. Green spheres: undercoordinated Si atoms; white: H atoms; gray: Cl atoms; red: vacancies. Bulk defects, i.e., Si atoms not belonging to the ideal crystal lattice, are superposed to the xyz data and represented as purple spheres.

4.3.2 KMCsL CVD simulations of Si nanoparticle

In this section we show that the atomistic framework can also be applied to simulate clean or defective CVD growth of nano-objects evolving in three dimensions. We consider an initially spherical Si nanocrystal with a 7 nm diameter (left panel in Figure 31) and carry out a clean CVD growth simulation of 36 s, which yields the expected reshaping into an energetically more favorable, {111}-faceted octahedral nanoparticle, often observed experimentally [22]. The same simulation carried out with `Ptranszig`=0.9 gives rise to a roughly octahedral nanoparticle with several stacking defects, in the form of triple stacking faults or local hexagonal crystalline domains (purple in Figure 31). The morphology and phase composition of the nanoparticle in actual experiments can be approximately reproduced by proper tuning of `Ptranszig` during calibration.
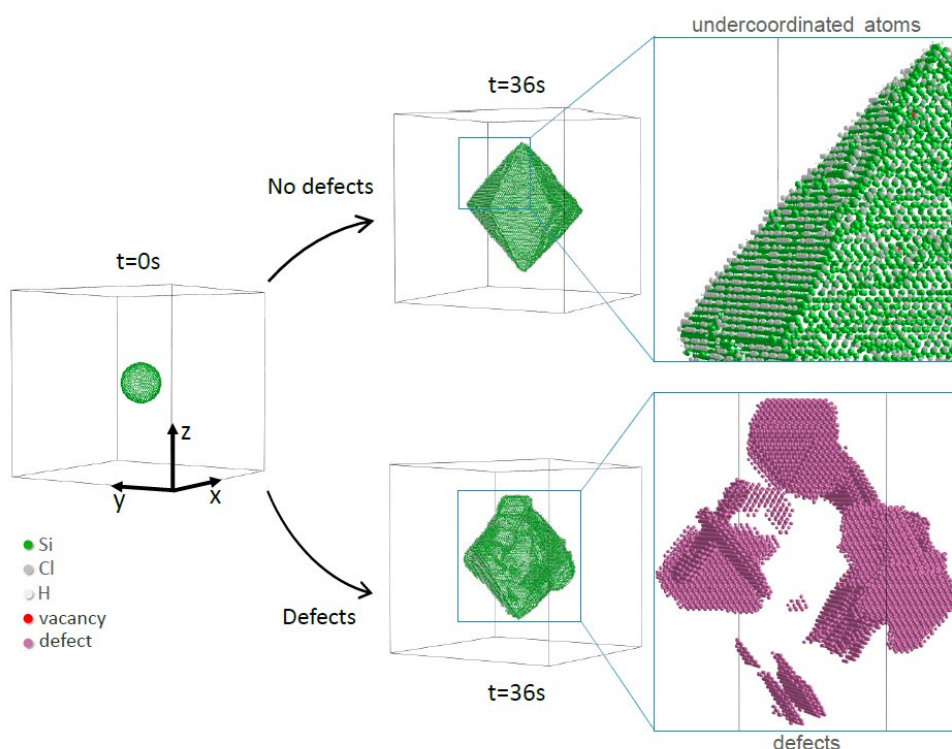

Figure 31: KMCsL simulation of CVD growth of a Si spherical nanoparticle, obtained imposing p_{H2} = 7813 Pa, p_{HCl} = 155 Pa, $p_{SiH2Cl2}$ = 31 Pa and T = 1263K, corresponding to gas-phase equilibrium precursors with p_{H2} = 7820 Pa, p_{HCl} = 148 Pa, p_{SiCl2} = 25 Pa. Left: input substrate geometry .xyz file. Right: crystal morphology after a 36 second simulated growth, in the absence of defects (upper structure, `Ptranszig`=1, the enlargement showing the crystal surface) and in their presence (lower structure, `Ptranszig`=0.9, the enlargement showing defective sites inside the crystal).

4.3.3   KMCsL CVD simulations of constrained Si nanocrystal

The CVD KMCsL simulation can be initiated from a TCAD input geometry. Non-evolving regions in the KMCsL box can be modeled as clusters of wall sites (see Section 4.1).

For example, in Figure 32 we consider an initial 5 x 5 x 3 nm^3 Si nanocrystal (blue in the bottom-left panel) lying on a non-evolving substrate and laterally constrained by a vertical non-evolving region (red in the bottom-left panel). The latter could represent, for instance, the insulating substrate and the gate stack in a FDSOI device geometry. The initial solid-gas interface in the KMCsL box at t=0, initializing the growth, is therefore a 3D roughly cubic nucleus. A clean CVD growth simulation yields the expected emergence of {111} faces. The same simulation carried out with `Ptranszig`=0.99 gives rise to a roughly similar behavior, but with several stacking defects and quite large hexagonal crystalline domains (purple atoms in Figure 32). Once again, `Ptranszig` can be tuned to achieve predictions in closer agreement with measured morphology and polymorphisms.
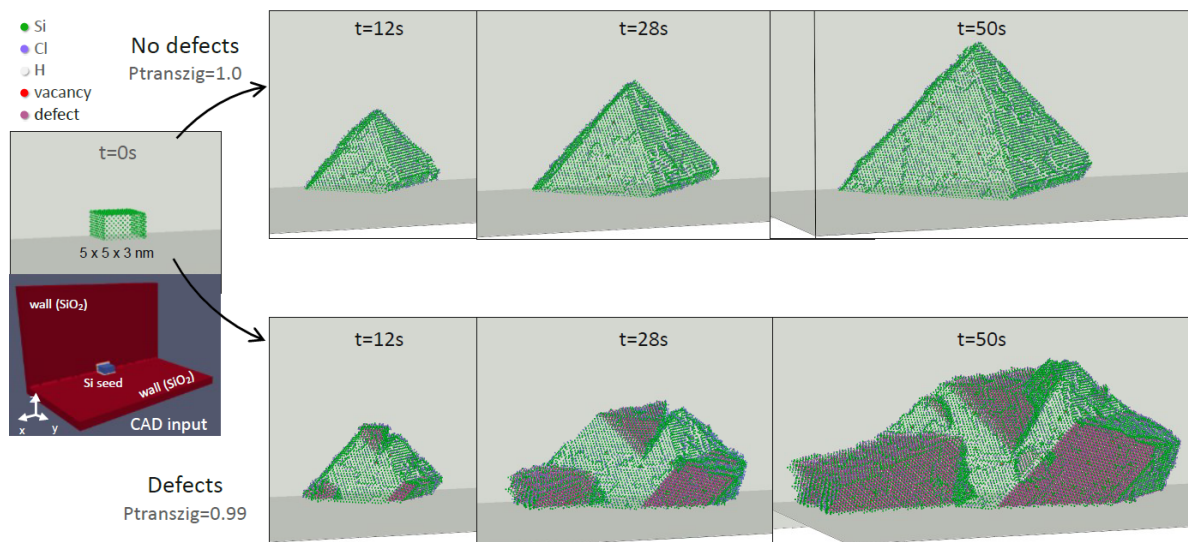

Figure 32: KMCsL simulation of CVD growth of a Si nanocrystal confined between two walls, obtained imposing p_{H2} = 7813 Pa, p_{HCl}=155 Pa, $p_{SiH2Cl2}$=31 Pa and T=1263K. Left : input substrate geometry, shown both as .xyz file (upper image, walls in gray) and as CAD structure (lower image, walls in red). Right: crystal morphology evolution during the growth, in the absence of defects (`Ptranszig`=1, upper structures) and in their presence (`Ptranszig`=0.99, lower structures). Green spheres: undercoordinated Si atoms; white: H; blue: Cl; red: vacancies; purple: bulk defects.

4.3.4   Other applications of the CVD KMCsL framework: the case of SiGe:B

The current CVD implementation in `MulSKIPS` allows up to 3 crystal species and 3 coverage species in the growth (etch) simulation. This is enough to reproduce typical precursor recipes of CVD processes for the most relevant elemental and binary semiconductors with tetrahedral bonding (SiGe, SiC, GaN, GaAs, InP, etc.), including dopant species (without diffusion or activation kinetics). The main requirement is the availability of a suitable set of experimental data and the appropriate calibration of kinetic parameters. More species may be added in future developments of the code. An example of KMCsL simulation of CVD growth of 30nm $Si_{1-x}Ge_x$:B layer on a Si(001) substrate, with the emergence of a triple stacking fault, is reported in Figure 33. The purpose of this simulation is only to demonstrate the extension capabilities of the developed atomistic CVD framework. An ad-hoc KMCsL parameter set was indeed designed without the use of CANTERA or benchmarks with experimental results, in order to reproduce the CVD growth of a layer with 30% Ge content and a B concentration of ~2.3E20 cm^{-3}.
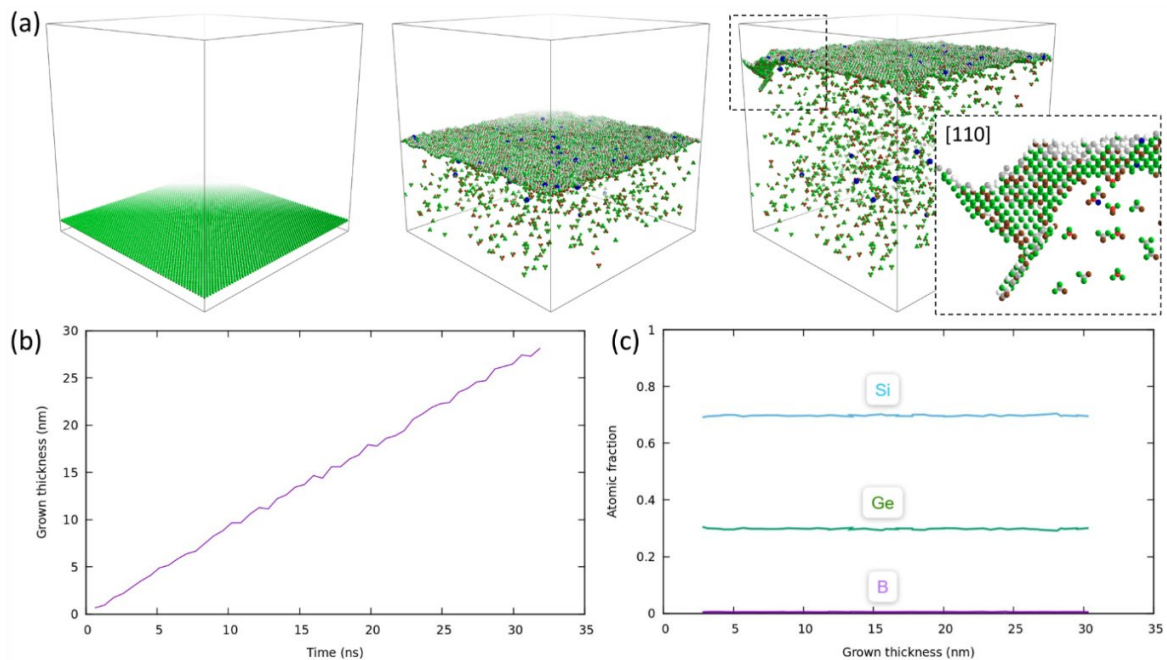

Figure 33: KMCsL simulation of CVD growth of 30nm $Si_{1-x}Ge_x$:B layer on a Si(001) substrate. An ad-hoc calibration was chosen, only for demonstration purposes, such to reproduce the growth of a layer with 30% Ge content and a B concentration of ~2.3E20 cm^{-3} (skipping the Cantera step of the workflow). (a) Snapshots of surface morphology during the growth. The [110] view in the inset shows a small stacking defect emerging during the simulation (`Ptranszig`=0.95). Si, Ge, B, H and Cl undercoordinated atoms are represented in green, brown, blue, white, and grey, respectively, while vacancies are in red. (b) Layer thickness over time. (c) Fraction of species in the layer as a function of layer thickness.

5. Post-epitaxy annealing

Usually, in a full process the epitaxial growth if followed by post-epitaxy anneals, leading to additional diffusion, changed activation, and relaxation of strain. This section is dedicated to the simulation of these post-epitaxial anneals and is based on work from Task 3.4.

5.1 Simulation setup

All simulations are obtained with the Sentaurus Process of Synopsys with AdvancedCalibration and AdvancedCalibration KMC [6, 7].

The 30 nm thick epitaxially grown SiGe layer is modeled by a deposition step on a Si substrate. The initial active B concentration is implemented as substitutional B, while the remaining, inactive concentration is assumed to be contained in B4 clusters. We note that it is crucial to deposit the SiGe layer as Si material with a SiGe mole fraction equal to the true experimental mole fraction. Using the SiGe material during deposition will lead to wrong sheet resistance values.

The Ge content of the SiGe layer and the total B concentrations have been measured with SIMS. The results are shown in Figure 34, for a more in-depth discussion see also D3.3. In addition, the activation for the three different total B concentrations has been measured by Hall measurements, see D3.5. These results are summarized in Table 10 and are used as initial conditions for the simulation.
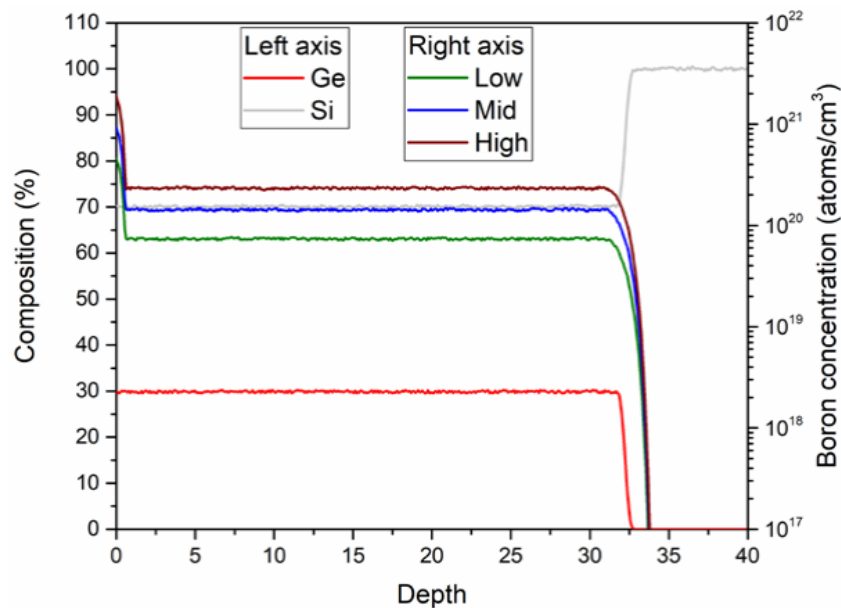

Figure 34: SIMS profiles depicting the composition of the SiGe layer (left axis) as well as the chemical B concentration for samples with low, mid, and high doping (right axis) as a function of depth.

Table 10: Overview of the B concentration and the activation for the three differently doped samples.

ID	Target B-conc (cm^{-3})	SIMS B-Conc at 15 nm (cm^{-3})	Activation (%)
Low	5×10^{18}	7.3×10^{19}	90
Mid	7×10^{19}	1.4×10^{20}	87
High	2.3×10^{20}	2.3×10^{20}	64

For the simulation of the laser annealing, CNR provided temperature vs time profiles for each laser pulse depending on the fluence. To speed up simulations the pulse data is interpolated so fewer points are necessary, while still ensuring the profiles' details. The profiles for fluences of 1.25 J/cm² and 1.35 J/cm² are shown in Figure 35. Here, the profile of lower fluence leads to a fully non-melt annealing. For the higher fluence, a plateau is visible at the profile's maximum, indicating that some melt occurs during this plateau.
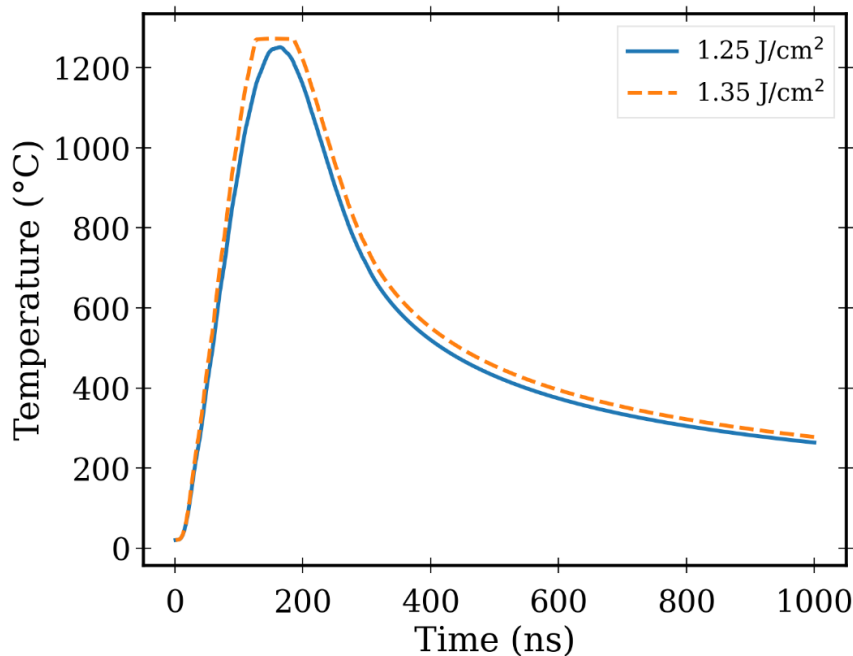

Figure 35: Simulated thermal profiles of single laser pulses used for annealing at fluences of 1.25 J/cm^2 and 1.35 J/cm^2.

Finally, to make the `SheetResistance` command work with KMC results, it is necessary to avoid regions with no doping, which can occur in the atomistic simulations. Therefore, we add a small background doping of 1×10^{12} cm^{-3} to the B doping profile obtained from KMC simulations. We then calculate the sheet resistance for the resulting profile.

5.2　Simulation results

In the following, we discuss the results from simulations set up as described in the section above. For the highly doped samples we can compare with experimental data from D3.5, while for the two samples with different doping, no experimental data is available, so we only show the results from simulation.
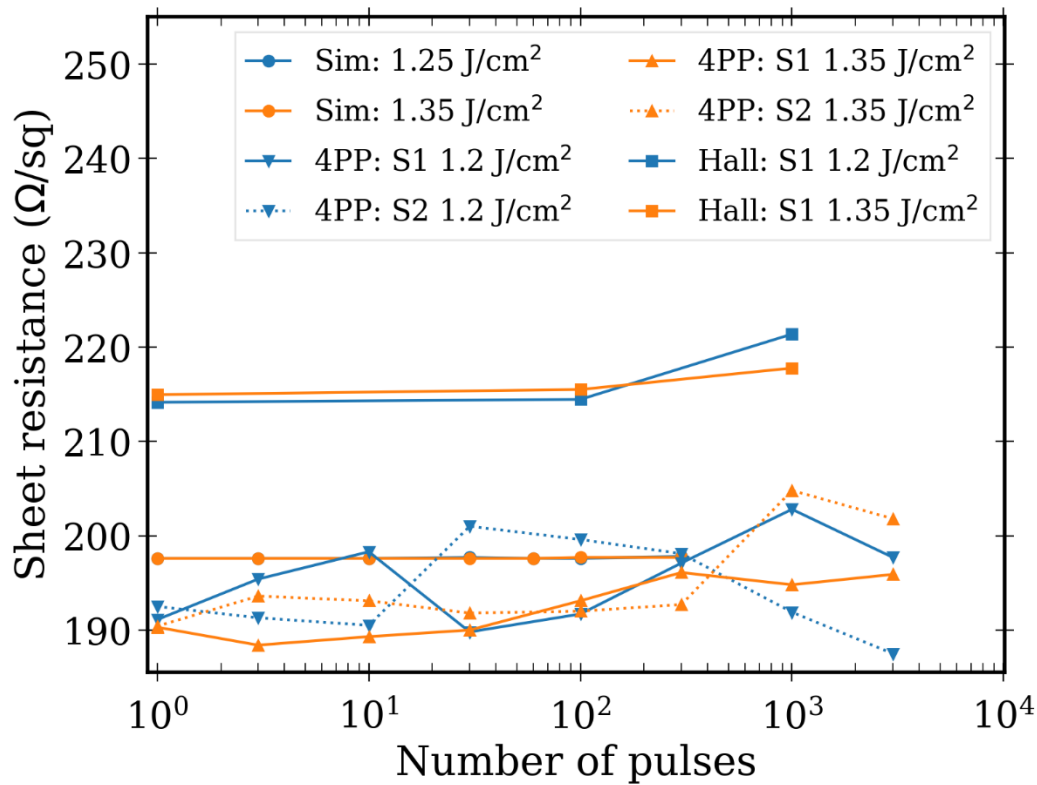
Figure 36: Sheet resistance as a function of the number of laser annealing pulses. Comparison between simulation, 4-point probe measurements, and Hall measurements for different fluences. S1 and S2 denote the sample that was measured. Both samples should be equal.

We first start with the highly doped samples to make sure that our simulation approach leads to viable data. In Figure 36 the sheet resistance is plotted as a function of the number of laser pulses used for annealing at different fluences. The two measurement methods predict mostly constant sheet resistances, which is also reproduced by simulation. Hall measurements show a sheet resistance of about $215 \, \Omega/sq$, while 4-point probe measurements (4PP) find sheet resistance varying in the range of $190 - 200 \, \Omega/sq$. Simulations predict a constant sheet resistance slightly above the 4PP measurement and right between the two measurement methods at about $197 \, \Omega/sq$. We thus find a great reproduction of experimental results.

In Figure 37 we show the simulation of the development of the sheet resistance (top) as well as the active B concentration (bottom) for the three different doping concentrations from Table 10, and the two different fluences (left/right). Again, we find that post-epitaxy sub-melt laser annealing has no influence on the activation of these layers. At low doping concentration we find sheet resistance of $412 \, \Omega/sq$, and at middle doping concentration, the sheet resistance is $235 \, \Omega/sq$.
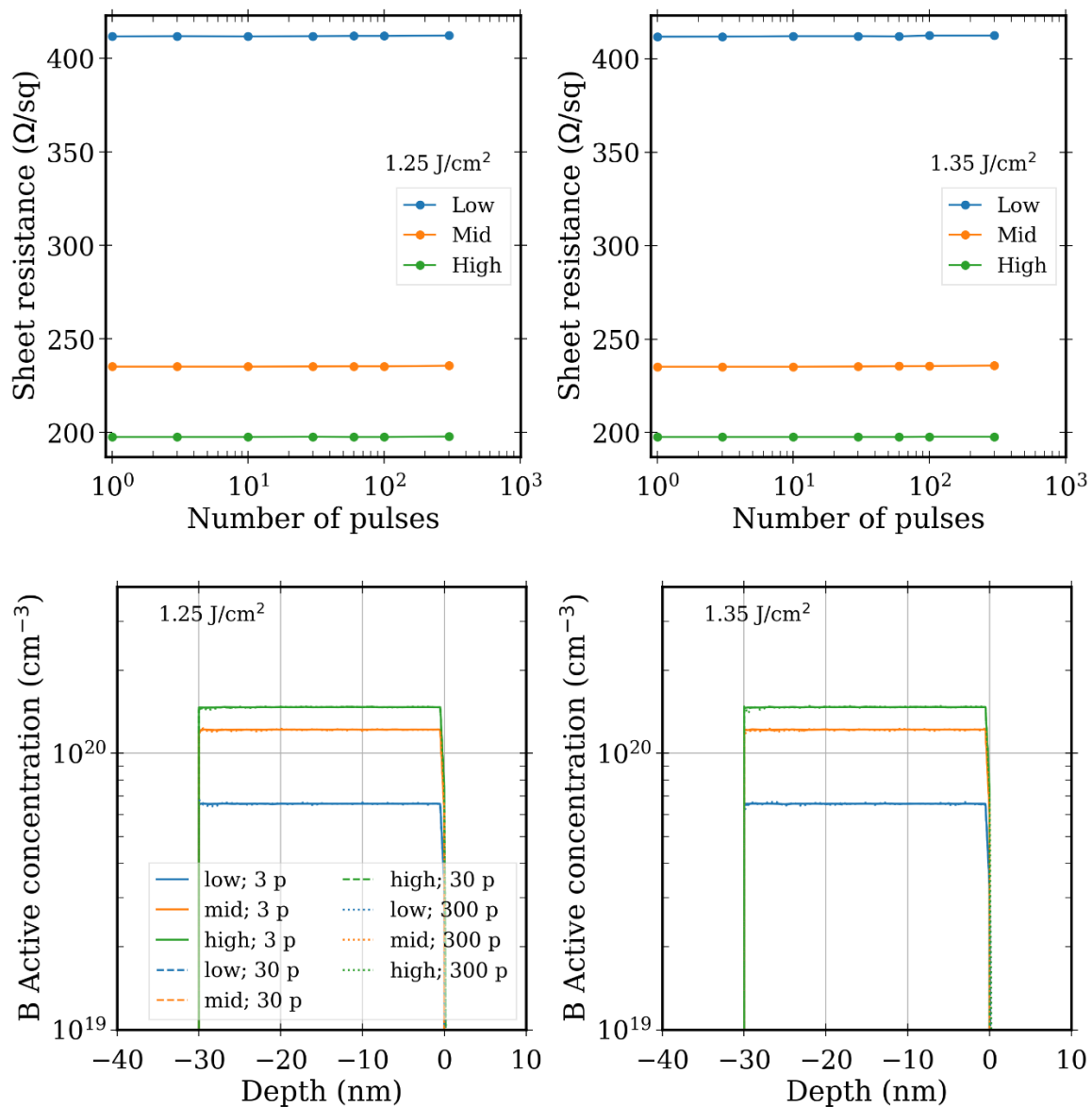
Figure 37: (top) Sheet resistance as a function of number of pulses at a fluence of (left) 1.25 J/cm² and (right) 1.35 J/cm² for low, middle, and high doping concentration. (bottom) Active B concentration as a function of depth for low, middle, and high doping concentration and different number of pulses at fluences (left) 1.25 J/cm² and (right) 1.35 J/cm².

Conclusions

In this deliverable of WP3, the final models for epitaxial growth and post-epitaxial annealing were described in detail. In the first step *ab initio* simulations of adsorption on Si(001) surfaces were discussed for hydrogen, silane and hydrogen chloride. Using CI-NEB it was possible to compute the reaction paths of silane adsorption with and without hydrogen coverage on the substrate. The same was done for silicon etching with HCl. Even though these *ab initio* simulations are limited to small parts of a full system, these results help with the calibration of LKMC simulations which are significantly faster and allow the simulation of larger systems but require a lot of calibration work to lead to reliable data. Within the MUNDFAB project, a dual approach was taken: Simulations are performed using the commercial TCAD tool Sentaurus

by Synopsys, as well as the open source tool `MulSKIPS`. This dual approach is also apparent in this deliverable, since the LKMC simulations of epitaxy are implemented in both tools and the results presented here.

For the implementation in Sentaurus, we focused on simulating six recipes that were provided by CEA. Three of these recipes are for the epitaxy of undoped SiGe layers with different mole fractions, while the other three are for *in situ* doped SiGe layers with different B concentrations. We calibrated the different precursors that are used for these recipes separately, including DCS, germane and HCl. These additional calibrations were then used to simulate the recipes. We found some problems with HCl, which cause nonphysical behavior leading to structural defective epi layers when it is included in a recipe. This is especially problematic for *in situ* doped recipes, which regularly include HCl. The consequences of these problems are atoms that are not attached to the surface, thick layers of passivating species beneath the surface, and rough surfaces in general. Additional calibration of HCl specific parameters could solve some of these problems but lead to new problems, like inconsistent etch rates. We therefore found the best way to simulate the *in situ* doped recipes is by not including HCl even though it is part of the recipe. This way we received structurally sound layers with good fits to the Ge content and B concentration but with too high growth rate.

The implementation of epitaxial growth in `MulSKIPS` is coupled to Cantera to also model gas-phase reactions. After calibration, the results from `MulSKIPS` for CVD epitaxy are compared to the experiment and an analytic solution of the epitaxial growth and one finds a very good reproduction of experimental results. Additional applications that were investigated are CVD epitaxy for a Si(001) surface with stacking defects, for a Si nanoparticle, for a constrained Si nanoparticle, and for boron-doped SiGe.

Finally, for the post-epitaxial anneals, we were able to reproduce the experimental results for the sheet resistance from D3.5. Just as in the experiment, we found that post-epitaxial laser annealing with sub-melt fluences has no significant impact on the activation of the dopants.

References

[1] P. Rosenow and R. Tonner, "Extent of Hydrogen Coverage of Si(001) under Chemical Vapor Deposition Conditions from Ab Initio Approaches," *J. Chem. Phys.,* vol. 144, p. 204706, 2016.

[2] L. Treps, J. Li and B. Sklénard, "Impact of Hydrogen Coverage on Silane Adsorption during Si Epitaxy from Ab Initio Simulations," *Solid-State Electronics,* vol. 197, p. 108441, 2022.

[3] J. Shi, E. S. Tok and H. Chuan Kang, "The dissociative adsorption of silane and disilane on Si(100)-(2×1)," *J. Chem. Phys.,* vol. 127, p. 164713, 2007.

[4] H. Park, E. Yoon, G.-D. Lee and H. J. Kim, "Analysis of Surface Adsorption Kinetics of SiH4 and Si2H6 for Deposition of a Hydrogenated Silicon Thin Film Using Intermediate Pressure SiH4 Plasmas," *Applied Surface Science,* vol. 496, p. 143728, 2019.

[5] B. Martinez, L. Treps, J. Li, H. Prats and B. Sklénard, ""Atomistic description of Si etching mechanism with HCl"," *(in preparation).*

[6] *Sentaurus Process User Guide, Version U-2022.12.*

[7] *Advanced Calibration for Process Simulation User Guide, Version U-2022.12.*

[8] J. M. Hartmann, M. Burdin, G. Rolland and T. Billon, "Growth kinetics of Si and SiGe on Si(100), Si(110) an Si(111) surfaces," *Journal of Crystal Growth,* vol. 294, pp. 288-295, 2006.

[9] J. M. Hartmann, V. Benevent, J. F. Damlencourt and T. Billon, "A benchmarking of silane, disilane and dichlorosilane for the low temperature growth of group IV layers," *Thin Solid Films,* vol. 520, pp. 3185-3189, 2012.

[10] J. M. Hartmann, A. Abbadie, M. Vinet, L. Clavelier und P. Holliger, „Growth kinetics of Si on fullsheet, patterned and silicon-on-insulator substrates," *Journal of Crystal Growth,* Bd. 257, pp. 19 - 30, 2003.

[11] J. M. Hartmann, L. Clavelier, C. Jahan, P. Holliger, G. Rolland, T. Billon und C. Defranoux, „Selective epitaxial growth of boron- and phosphorus-doped Si and SiGe for raised sources and drains," *Journal of Crystal Growth,* Bd. 264, pp. 36 - 47, 2004.

[12] Y. Bogumilowicz, J. Hartmann, R. Truche, Y. Campidelli, G. Rolland und T. Billon, „Chemical vapour etching of Si, SiGe and Ge with HCl; applications to the formation of thin relaxed SiGe buffers and to the revelation of threading dislocations," *Semiconductor Science and Technology,* Bd. 20, pp. 127 - 134, 2005.

[13] J. M. Hartmann, V. Destefanis, G. Rabillé und S. Monfray, „HCl selective etching of SiGe versus Si in stacks grown on (110)," *Semiconductor Science and Technology,* Bd. 25, pp. 105009 - 105018, 2010.

[14] G. Calogero, G. Fisicaro, I. Deretzis and A. La Magna, "MulSKIPS: A Kinetic Monte Carlo super-Lattice code designed to simulate with atomic resolution the kinetics of processes," 2023. [Online]. Available: https://github.com/MulSKIPS. [Online].

[15] G. Fisicaro, C. Bongiorno, I. Deretzis, F. Giannazzo, F. La Via, F. Roccaforte, M. Zielinski, M. Zimbone and A. La Magna, "Genesis and evolution of extended defects: The role of evolving interface instabilities in cubic SiC," *Appl. Phys. Rev.,* vol. 7, p. 021402, 2020.

[16] G. Calogero, D. Raciti, P. Acosta-Alba, F. Cristiano, I. Deretzis, G. Fisicaro, K. Huet, S. Kerdilès, A. Sciuto and A. La Magna, "Multiscale modeling of ultrafast melting phenomena," *npj Computational Materials,* vol. 8, p. 36, 2022.

[17] A. La Magna, A. Alberti, E. Barbagiovanni, C. Bongiorno, M. Cascio, I. Deretzis, F. La Via and E. Smecca, "Simulation of the Growth Kinetics in Group IV Compound Semiconductors," *Phys. Stat. Sol. A,* vol. 216, p. 1800597, 2019.

[18] D. G. Goodwin, H. K. Moffat, I. Schoegl, R. L. Speth and B. W. Weber, "Cantera: An object-oriented software toolkit for chemical kinetics, thermodynamics, and transport processes," 2022. [Online]. Available: https://www.cantera.org. [Accessed 2023].

[19] B. J. McBride, M. J. Zehe and S. Gordon, "NASA Glenn Coefficients for Calculating Thermodynamic Properties of Individual Species," 2002. [Online]. Available: https://ntrs.nasa.gov/citations/20020085330. [Accessed 2023].

[20] Q. Gao, C. C. Cheng, P. J. Chen, W. J. Choyke and J. T. Yates Jr., "Comparison of Cl2 and HCl adsorption on Si(100)-(2x1)," *Thin Solid Films,* vol. 225, pp. 140-144, 1993.

[21] P. A. Coon, M. L. Wise and S. M. George, "Modeling silicon epitaxial growth with SiH2Cl2," *Journal of Crystal Growth,* vol. 130, pp. 162-172, 1993.

[22] G. Mannino, A. Alberti, R. Ruggeri, S. Libertino, A. R. Pennisi and G. Faraci, "Octahedral faceted Si nanoparticles as optical traps with enormous yield amplification," *Scientific Reports,* vol. 5, p. 8354, 2015.